Contributions to Mineralogy and Petrology (2021) 176:90
https://doi.org/10.1007/s00410-021-01844-y

ORIGINAL PAPER

Evidence for polybaric fractional crystallization in a continental arc: Hidden Lakes mafic complex, Sierra Nevada batholith, California

Madeline J. Lewis[1] · Claire E. Bucholz[1] · Oliver E. Jagoutz[2]

Received: 14 January 2021 / Accepted: 15 September 2021

Abstract

Although the voluminous granitoids that constitute the upper crust of the Sierra Nevada batholith (California) have been investigated in detail, comparatively few studies focus on the origin of mafic bodies at similar crustal levels. Here, we present field and petrographic observations, geochronology, and geochemistry of the Hidden Lakes mafic complex in the central-eastern Sierra Nevada batholith. Our results show that the complex comprises norites, gabbros, monzondiorites, and monzonites that record fractional crystallization of a hydrous (~ 3 wt% H_2O), non-primitive basalt within the upper crust (0.3 GPa) at c. 95–96 Ma. To quantitatively model the generation of the observed lithologies, we construct a two-stage polybaric crystallization model based on cumulate and melt-like bulk-rock compositions. In the first step, we model fractionation of a primitive, mantle-derived basalt at > 30 km depth, generating dominantly pyroxenite cumulates. The evolution of the derivative melt (67% of melt mass remaining) is then modeled to fractionate at 12 km depth to produce the observed lithologies within the Hidden Lakes mafic complex. Extension of this model to higher-silica melt compositions (> 65 wt% SiO_2) replicates observed granodiorite compositions in the batholith, suggesting that polybaric crystallization could be an important process for the generation of arc granitoid melts. The depth of differentiation in continental arcs is debated, as field observations indicate abundant lower crustal fractionation while experimental data suggest that high-pressure crystallization of hydrous basalts cannot produce the non-peraluminous granitoid compositions observed in continental arc batholiths. Our model supports polybaric differentiation as one potential mechanism to resolve this inconsistency.

Keywords Mafic · Gabbro · Sierra Nevada batholith · Polybaric · Arc · Fractional crystallization

Introduction

The generation of batholith-scale granodiorite intrusions in continental arc settings is an unresolved problem, as differentiation mechanisms produce only small volumes of granitic melt (~ 10–20% of original melt mass) in comparison to much greater volumes of ultramafic and mafic cumulates or restites (Kay and Kay 1985; Soesoo 2000; Jagoutz and Klein 2018). However, lower crustal mafic and ultramafic cumulates are ubiquitous in magmatic arcs exhumed to 30–55 km depths (Debari and Sleep 1991; Greene et al. 2006; Jagoutz et al. 2009; Jagoutz 2010, 2014; Otamendi et al. 2012; Walker et al. 2015; Guo et al. 2020) and may be brought to the surface as xenoliths in active volcanic arcs (Debari et al. 1987; Arai and Ishimaru 2008). Therefore, magmatic differentiation by lower crustal fractional crystallization of hydrous basalts is considered an important process in the formation of granodiorites and granites characteristic of the upper crust (Greene et al. 2006; Otamendi et al. 2012; Jagoutz 2014; Walker et al. 2015; Guo et al. 2020). Experimental studies (Müntener et al. 2001; Sisson et al. 2005; Nandedkar et al. 2014; Müntener and Ulmer 2018; Ulmer et al. 2018) and thermodynamic modeling (Annen et al. 2006; Jagoutz and Klein 2018) also support the hypothesis that deep (> 0.7 GPa) differentiation of hydrous basalts can produce high-silica melts.

However, detailed experimental high-pressure crystallization studies suggest that differentiation in the deep crust

Communicated by Othmar Müntener.

✉ Madeline J. Lewis
maddie@purdue.edu

[1] Division of Geological and Planetary Sciences, California Institute of Technology, Pasadena, CA, USA

[2] Department of Earth, Atmospheric, and Planetary Sciences, Massachusetts Institute of Technology, Cambridge, MA, USA

Published online: 15 October 2021

cannot be solely responsible for the compositional stratification observed in arcs. Crystallization of hydrous primitive basalts in the lower crust (i.e., > 0.7 GPa) produces peraluminous andesites, which are rarely observed in arc batholiths (Cawthorn and Brown 1976; Cawthorn and O'Hara 1976; Blatter et al. 2013; Nandedkar et al. 2014; Melekhova et al. 2015; Müntener and Ulmer 2018; Ulmer et al. 2018). Although the experimental basalts used in some of these studies are Al enriched, their starting compositions are within the range of observed primitive arc basalts, as compiled by Schmidt and Jagoutz (2017). At lower crustal pressures and high (≥ 2 wt%) water contents, suppression of plagioclase and abundant early clinopyroxene crystallization drives residual melts toward peraluminous compositions (i.e., ASI > 1.1 where ASI = molar Al/(Ca-1.67 × P + Na + K). In contrast, at lower pressures (< 0.7 GPa) and/or lower water contents plagioclase and orthopyroxene (in the case of lower water activities) will saturate in a basalt at higher temperatures, limiting the increases in ASI in a crystallizing melt. As supported by high-pressure experimental studies, differentiation in arcs is not a simple story of high-pressure differentiation.

Thus, there are two observations that must be reconciled: (1) lower crustal arc sections dominated by ultramafic to mafic cumulates indicating the importance of deep crustal fractional crystallization and (2) experimental crystallization studies suggesting that although high-silica melts can be produced at these pressures, they will become peraluminous at relatively low SiO_2 contents (< 60 wt%), a feature rarely observed in arc batholiths. Three processes have been proposed to explain this apparent contradiction: (1) polybaric differentiation (Hamada et al. 2014; Melekhova et al. 2015), (2) mixing between low-Mg basaltic and granitic melts (Sisson et al. 1996, 2005; Grove et al. 2003; Blatter et al. 2013; Müntener and Ulmer 2018), or (3) mixing of dry and wet magmas to produce "damp" (< 2 wt% H_2O) basalts to andesites that then further differentiate in the lower crust (e.g., Sisson et al. 2005; Müntener and Ulmer 2018; Rezeau et al. 2021). All three of these processes require the presence of evolved (low-MgO) basalts produced through lower crustal differentiation of more primitive, high-MgO basalts. However, each is not without its shortcomings. In scenario (1), the low-MgO basalts can ascend into the upper crust to differentiate further, producing non-peraluminous silicic melts. The absence of significant volumetrically significant mafic plutons in the upper crust of exposed arcs, however, suggests that this may be relatively minor process. In scenario (2), the low-MgO basalts mix with higher-silica melts (formed through fractional crystallization, partial melting, or both) to produce granodioritic magmas. However, mixing of two magmas with strongly contrasting viscosities is mechanically unviable (Sparks and Marshall 1986). Last, in scenario (3), the low-MgO basalts with variable water contents mix to produce a damp (< 2 wt% H_2O) basalt that then differentiates in the lower crust without significant alumina enrichment due to early orthopyroxene and plagioclase crystallization. However, although crystallization of damp basalts in the lower crust can ameliorate issues with ASI increases during differentiation, this model cannot explain other features of arc batholiths. For example, dry to damp differentiation of basalts will follow a tholeiitic trend (increasing FeO/MgO with SiO_2) which is not observed in the calc-alkaline batholiths of continental arcs (e.g., Villiger et al. 2004; Melekhova et al. 2015; Müntener and Ulmer 2018).

To test whether these processes play an important role in the generation of arc batholiths, this study focuses on an upper crustal mafic complex in a continental arc batholith. Although less common than voluminous silicic plutons, upper crustal mafic intrusions potentially preserve information on the nature and origin of low-MgO basalts in the formation of arc batholiths. Here, we undertake a case study of the Hidden Lakes mafic complex (HLMC), an exposure of norite through monzonite emplaced into the upper crust of the Sierra Nevada batholith. We present detailed field mapping to document intrusive relationships and the range of mafic lithologies, and U–Pb zircon geochronology to determine the timing of crystallization of the HLMC relative to surrounding high-silica intrusions. Using bulk-rock and mineral chemistry data, as well as comparisons to experimental studies, we aim to constrain crystallization pressures, temperatures, H_2O content, and oxygen fugacity (fO_2) of the crystallizing magma. As field, petrographic, and geochemical data suggest a fractional crystallization origin for the HLMC, we construct a two-stage polybaric fractionational crystallization model to replicate the composition of the evolving melt. In light of our findings, we discuss the importance of evolved basalts in the formation of high-silica arc batholiths.

Geologic setting

The HLMC is located in the eastern central Sierra Nevada batholith (SNB), the largely granodioritic intrusive product of the Sierra Nevada paleo-continental arc. From the late-Triassic through late-Cretaceous, magmatism related to subduction of the Farallon plate beneath North America produced felsic intrusions that now form the bulk of the batholith. Magmatism ceased by 75 Ma due to shallowing of the subduction angle (English et al. 2003; Kirsch et al 2016). Presently, most of the SNB is exposed to upper crustal depths (0.2–0.4 GPa), with the exception of the southernmost lower crustal section which extends to 1.0 GPa pressures (Ague and Brimhall 1988; Pickett and Saleeby 1993). The late-Jurassic (145–160 Ma) and late-Cretaceous (85–100 Ma) periods in the SNB are characterized by enhanced magmatic activity, during which of 85% of

the batholith volume was generated (DeCelles et al. 2009; Ducea et al. 2015; Kirsch et al. 2016).

Numerous mafic bodies throughout the SNB upper crust were noted during early studies of the batholith (Mayo 1941; Bateman and Eaton 1967; Frost 1987), but have been less comprehensively studied as compared to the felsic batholith due to their relatively small areal fraction of the exposed SNB. Geochronological studies on a few of the mafic bodies demonstrate that they are coeval with the surrounding granitoids and therefore may play a critical role in the formation of the granitoid batholith (Coleman et al. 1995; Ratajeski et al. 2001). Several mafic bodies have been investigated in previous studies (Frost 1987; Frost and Mahood 1987; Coleman et al. 1995; Sisson et al. 1996; Ratajeski et al. 2001; McCarthy and Müntener 2016), all of which document the presence of hydrous, low-Mg basalts in the upper crust of the SNB.

Field relationships

The Hidden Lakes mafic complex (HLMC) is exposed in the central SNB near Bishop, CA, and covers an area of 2.5 km^2. Our field mapping (Fig. 1) refines the outer margins of the mafic complex where it is in contact with surrounding granodiorite plutons, as previously mapped by Bateman (1992), and displays the variation in rock types and the nature of contacts within the mafic complex. Amphibole- and biotite-bearing medium- to fine-grained gabbros are the dominant

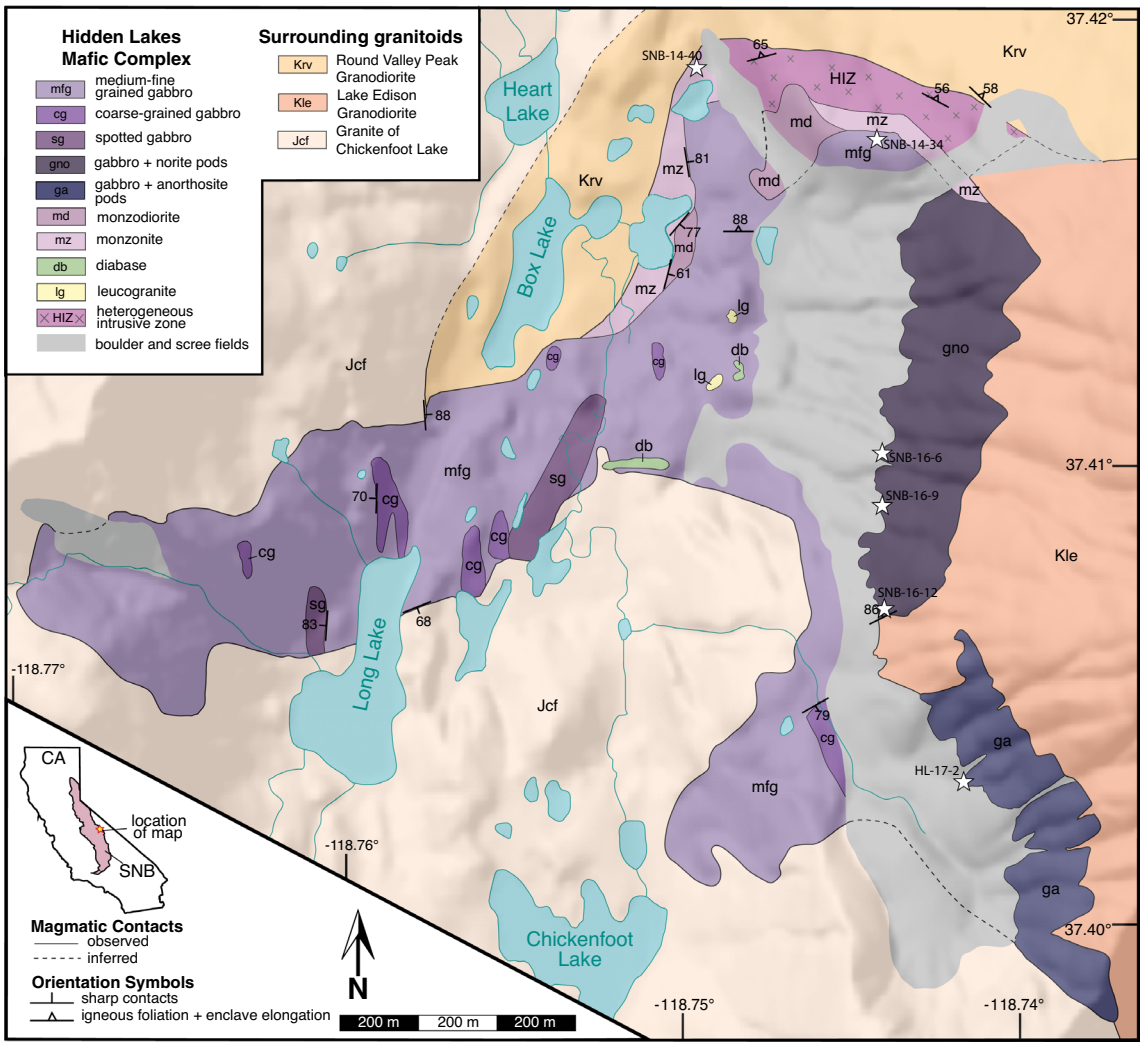

Fig. 1 Geologic map of the Hidden Lakes mafic complex study area and surrounding granite and granodiorite plutons, located in the central Eastern Sierra Nevada Mountains. Star symbols mark the locations of samples used for geochronology, and sample numbers are shown adjacent to the symbols. See Supplementary Material for all sample GPS locations. Contacts within HLMC and those that define the boundary of the mafic complex are based on our own field mapping. Some contacts may be gradational over several meters, as described in the text, but are indicated by sharp contacts here. Locations of contacts between the felsic plutons (Kle, Krv, and Jcf) are based on Bateman (1992)

lithology throughout HLMC. Norites occur as small pods within the gabbro in the eastern section of HLMC. In the northeastern section of HLMC, near its contact with the Round Valley Peak granodiorite, lithologies transition gradationally from gabbro to monzodiorite to monzonite toward the northern edge of the mafic complex. The field occurrences and characteristics of each rock type in the mapped area are described in detail below.

Norites

Norites are the most primitive lithology found in HLMC and are present as small, rounded pods (up to 3 m) within the gabbro unit in the eastern section of the complex (Fig S2a). Their volumetric abundance within the gabbro is difficult to ascertain due to exposure on steep cliff faces; however, they weather out and occur as large boulders in the scree fields to the west of the cliffs. Norite boulders are significantly less abundant in scree fields than gabbro boulders, so it is presumed that norite is less common than gabbro in the cliff exposures.

Anorthosites

Anorthosite was observed only in rare boulders below gabbro-dominated cliffs in the southeastern section of HLMC (Fig. 1). The anorthosite is medium–fine-grained (0.5–2 mm), isotropic, and contains 90–95% dark gray plagioclase with 5–10% biotite.

Gabbros

Amphibole-biotite gabbro is the volumetrically dominant rock type in HLMC and is present in most areas of the mafic complex, except for the northern margin characterized by more evolved lithologies (Fig. 1). The gabbros contain abundant plagioclase and amphibole, along with common clinopyroxene and biotite, and minor orthopyroxene. Based on their macroscopic textures, the gabbros are divided into three main groups: (1) medium–fine-grained gabbro, (2) coarse-grained gabbro, and (3) "spotted" gabbro (Fig S2).

Medium–fine-grained gabbro is the most common rock type in HLMC and contains dark gray plagioclase, amphibole, and pyroxene (1–3 mm) with evenly distributed finer-grained biotite (~ 1 mm). The coarse-grained gabbro is present in elongate bodies within the medium–fine-grained gabbro (Fig. 1). The mineral assemblage in the coarse-grained gabbro is identical to the medium–fine-grained gabbro, with slightly less plagioclase. The "spotted" gabbro is characterized by 1–2 cm clots of poikilitic amphibole + biotite enclosing pyroxene and minor plagioclase, which give it a spotted surface appearance (Fig S2). Clots are enclosed in a finer-grained matrix that is mineralogically very similar to the medium–fine-grained gabbro.

Contacts between the different textural gabbroic units are gradational over 1–5 m, or can exhibit mingling textures. Elongate intrusion geometry is evident in the western and southern areas of HLMC, while the eastern section appears to be a single large intrusion composed mainly of medium–fine-grained gabbro that grades into monzodiorite to the northeast.

Monzodiorites and monzonites

In the northeastern section of HLMC, two bodies of monzodiorite and two elongate bodies of monzonite are in largely gradational contact with one another over > 5 m. Mingling textures between the monzonite and monzodiorite, as well as dikes of monzonite intruding into monzodiorite, and vice versa, are present. Thus, these are synmagmatic lithologies that were mobilized shortly after crystallization of the northeastern section of gabbro.

The monzodiorites are medium-fine grained, dominated by plagioclase, and contain biotite, K-feldspar, amphibole, and interstitial quartz in order of decreasing abundance. Rare clinopyroxene is present in the cores of amphibole grains. The monzonites are typically medium to coarse grained, dominated by plagioclase and clusters of biotite + amphibole. K-feldspar is more common than in the monzodiorites, and quartz is typically minor and interstitial.

Diabase bodies

Generally small, irregularly shaped bodies of diabase, as well as diabase dikes, are present within and near HLMC. Intrusions are fine grained and occasionally contain blocks of HLMC gabbro. Contacts between the diabase and the mafic complex are sharp, in contrast with the generally gradational contacts between the coarser-grained lithologies, suggesting that the diabase is significantly younger than much of HLMC.

Surrounding felsic plutons and outer contacts

Three felsic intrusions are in contact with the HLMC around its perimeter: the granite of Chickenfoot Lake to the west and south, the Lake Edison granodiorite to the east, and the Round Valley Peak granodiorite (Krv) to the north (Fig. 1).

The granite of Chickenfoot Lake (Jcf, 191.6 ± 1.0 Ma, this study) is one of few Jurassic-aged plutons in the central SNB. Where observed, the contact between Jcf and HLMC is a 0.1–1 m wide gradational zone of dioritic composition

that occasionally includes coarse orthoclase xenocrysts, which are not present in the adjacent gabbros and so presumably originated as crystals in Jcf (Fig S3b). Diorite dikes originating from HLMC intrude into the Jcf. The Lake Edison granodiorite (Kle, 90.9 ± 0.1 Ma; Lackey et al. 2008) intrudes HLMC on its eastern side, creating a subvertical and sharp contact with Kle truncating layering in HLMC. The Round Valley Peak granodiorite (Krv) intruded at 88.8 ± 0.02 Ma (Lackey et al. 2008) and forms a complicated contact zone (the Heterogeneous Intrusive Zone) where it intrudes the northeastern margin of HLMC.

Heterogeneous intrusive zone

The east–west trending contact between Krv and HLMC is a ~ 150 m wide contact zone, which we term the Heterogeneous Intrusive Zone (HIZ). This zone consists of a magmatic breccia composed of 50–85% Krv granodiorite that has entrained angular to subangular blocks of gabbro, monzodiorite, and monzonite. Mafic blocks vary in size (5 cm–10 m) and angularity with the most angular blocks present on the southern margin of HIZ. Blocks become progressively more rounded and partially digested toward the north (Fig S3c). Meter to sub-meter scale dikes of the Krv intrude the HLMC immediately south of the HIZ, and sometimes contain angular xenoliths of gabbro, monzodiorite, and monzonite from the HLMC (Fig S3d).

Petrography

Descriptions of 28 representative samples in thin section are given below, with at least three sections from each rock type. Modal percent of major minerals were estimated visually (Table 1).

Norites

The norites consist of orthopyroxene (15–75%), plagioclase (15–40%), amphibole (0–20%), biotite (5–15%), clinopyroxene (1–5%), and olivine (< 1%), along with minor Fe-Ti oxides and accessory apatite and zircon. Norite samples exhibit ad- and mesocumulate textures with rounded orthopyroxene grains that range in size from 50 to 600 µm (Fig. 2a). All samples contain interstitial plagioclase and few contain euhedral plagioclase crystals ranging from 0.2 to 3 mm. Amphibole occurs either as large oikocrysts (1 cm) enveloping orthopyroxene and plagioclase ± olivine (Fig. 2b), or as overgrowths on orthopyroxenes and clinopyroxenes (Fig S4a). Late crystallizing biotite (0.4–2 mm) fills interstitial spaces and surrounds rounded orthopyroxenes. Olivine was observed in two samples (0.2–1 mm). Minor Fe and Fe-Ti oxides are included in orthopyroxene and plagioclase.

Gabbros

The relative proportions of mineral phases in the gabbros are variable, with the following ranges: plagioclase 45–75%, amphibole 5–50%, clinopyroxene 5–20%, biotite 5–10%, and orthopyroxene 0–5%. Gabbros with both cumulative and non-cumulative textures are present in HLMC (Fig. 2c, d). Coarse-grained and spotted gabbro samples, as well as some of the medium–fine-grained gabbros, preserve textural evidence for accumulation of plagioclase and clinopyroxene. These meso- to adcumulate samples are dominated by equant, nearly euhedral plagioclase (0.5–4 mm) and rounded clinopyroxene (0.5–3 mm) crystals. Orthopyroxene is far less prevalent than clinopyroxene, and both pyroxenes commonly contain exsolution lamellae. Amphibole is present as a primary magmatic phase, secondary magmatic rims nucleated on pyroxenes, and as psuedomorphs after pyroxene (Fig. 2c, Fig S4b). Biotite is a late crystallizing interstitial phase containing inclusions of clinopyroxene, plagioclase,

Table 1 Summary of modal mineralogies

	Norite	Gabbro (coarse-grained)	Gabbro (medium-fine-grained)	Monzodiorite	Monzonite	Anorthosite
Olivine	0–< 1[a]	–	–	–	–	–
Orthopyroxene	15–75	–	~ 5	–	0–< 1	–
Clinopyroxene	1–5	5–20	5–15	0–2	0–< 1	–
Plagioclase	15–40	45–70	65–75	60–70	40–60	90–95
Amphibole	0–20	25–50	5–20	5–15	0–5	–
Biotite	5–15	5–10	5–10	15–20	10–20	5–10
K-feldspar	0–< 1	< 1	< 1	10–15	20–35	–
Quartz	–	–	–	0–2	0–5	–

[a]All modal mineralogies are given in percent and estimated visually, with ranges reflecting variability within each lithologic group. Uncertainties are roughly 10% of reported values

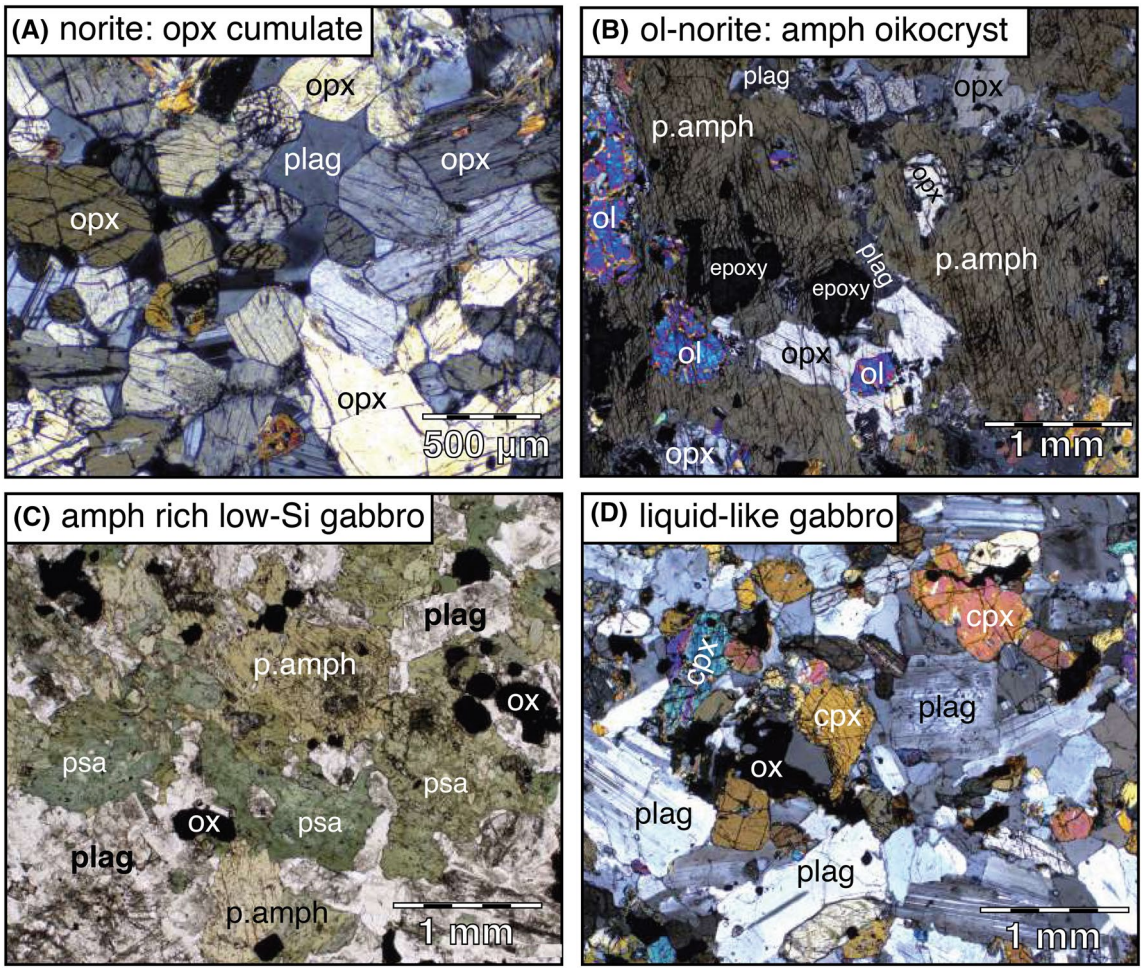

Fig. 2 Photomicrographs of norite and gabbro textures. **a**, **b**, and **d** were taken in cross-polarized light. **c** was taken in plain-polarized light. Mineral abbreviations: p.amph = primary magmatic amphibole, psa = pseudomorphic amphibole (pyroxene replacement), cpx = clinopyroxene, opx = orthopyroxene, plag = plagioclase, ox = Fe-Ti-oxide, ol = olivine. **a** Opx-rich norite adcumulate with interstitial plagioclase, SNB-14-59. **b** Poikolitic amphibole-bearing norite with olivine and orthopyroxene chadacrysts within coarse amphibole oikocryst, SNB-14-62. **c** Amphibole-rich medium-fine grained gabbro with both primary magmatic amphibole (amber colored), pseudomorphic amphibole (green), plagioclase, and Fe-Ti-oxides, SNB-18-3. **d** Medium-fine grained gabbro with clinopyroxene, plagioclase, and Fe-Ti-oxides, representative of a non-cumulate texture, SNB-14-54

and Fe–Ti oxides. Small, rare alkali feldspars are present interstitially.

Monzodiorites and monzonites

The monzodiorites and monzonites of HLMC are distinguished from the gabbros by a decreased abundance of pyroxene, though many monzodiorites contain pseudomorphs of pyroxene altered to amphibole. These pseudomorphs occasionally have ortho- and clinopyroxene cores. The monzodiorites consist of 60–70% plagioclase, 15–20% biotite, 10–15% K-feldspar, 5–15% amphibole, < 2% quartz, and minor ortho- and clinopyroxene (0–2%). All three occurrences of amphibole are common (primary magmatic, secondary magmatic, and pseudomorphic). Amphibole, biotite, and Fe–Ti oxides are often found together in 1–3 mm clots (Fig S4c).

The monzonites contain 40–60% plagioclase, 20–35% K-feldspar, 10–20% biotite, 0–5% amphibole, and minor quartz (< 5%). Euhedral to subhedral primary magmatic amphibole grains (0.3–1.5 mm) lie between generally coarse anhedral plagioclase and K-feldspars. Irregularly shaped flakes of biotite (0.5–2 mm) are packed between plagioclase crystals and can be included in K-feldspars (Fig S4d). Quartz (up to 0.5 mm) occurs interstitially.

Results

Zircon U–Pb isotopic measurements, bulk-rock major and trace element concentrations, and mineral chemistry data are included along with sample GPS locations in the Supplementary Data File (Tables S1–S3). Analytical methods are described in the Supplementary Material.

Geochronology

Zircon from six total samples of monzodiorite and monzonite from the HLMC were dated using laser ablation inductively coupled mass spectrometry (LA-ICPMS) at the University of California, Santa Barbara, and one granite sample was dated using LA-ICPMS at the Arizona Laserchron Center. All dated HLMC samples (not including the granite sample) are late Cretaceous in age. Weighted mean crystallization ages and 2σ errors for monzodiorite samples are 95.1 ± 1.0 Ma for SNB-16-6, 95.6 ± 0.8 Ma for SNB-16-9, and 96.5 ± 0.8 Ma for SNB-14-34. HL-17-2, an anorthosite, has an age of 95.7 ± 0.7 Ma. The monzonite ages are 96.3 ± 0.8 Ma for SNB-16-12 and 90.5 ± 0.8 Ma for SNB-14-40. These ages allow for up to 6 Ma of magmatic activity in HLMC and constrain crystallization ages of the more mafic parts of the HLMC at 5 and 7 million years older than the Lake Edison granodiorite (90.9 ± 0.1 Ma; Lackey et al. 2008) and Round Valley Peak granodiorite (88.8 ± 0.02 Ma; Lackey et al. 2008), respectively. HLMC is significantly younger than the granite of Chickenfoot Lake (at 191.6 ± 1.0 Ma, this study). These ages are consistent with field relationships, in which HLMC lithologies are observed intruding into Jcf and intruded by Kle and Krv. Sample SNB-14-40, a monzonite from the northern edge of the mafic complex near the contact with Krv, has a crystallization age ~ 5 Ma younger than the other five mafic samples (90.5 ± 0.8 Ma). This may represent a late-stage melt associated with differentiation of HLMC magmas that was remobilized by intrusion of Kle, as their ages overlap within uncertainty. We presume that the gabbros and norites crystallized within the range of monzodiorite ages (95.1–96.5 Ma), though neither of these more mafic lithologies were directly dated due to the rarity of zircon.

Bulk-rock major element chemistry

Major element bulk compositions from HLMC were analyzed via X-ray fluorescence (XRF) spectrometry at Caltech, following methods in Bucholz and Spencer (2019). Samples display a trend of magmatic evolution that straddles the boundary between a monzonitic series and granodioritic series (Bas et al. 1986; Middlemost 1994). For simplicity, we retain the lithology names norite, gabbro, monzodiorite, and monzonite as classified based on mineralogy in previous sections, even if all samples of one lithology do not fit precisely within a single chemically defined field (Fig. 3a). SiO_2 contents from the full suite of HLMC samples range from 43.6 to 62.0 weight percent (wt%) and molar Mg numbers (Mg# = 100 × Mg/[Mg + Fe], calculated using total Fe) range from 73 to 46 (Fig. 3d). Aluminum saturation index (ASI) values of HLMC samples range from 0.57 to 0.96 (ASI = Al/[Ca-1.67 × P + Na + K]), indicating that all sampled lithologies are metaluminous.

The norites represent the most primitive cumulates to crystallize from an HLMC melt, based on their high Mg#s (73.1–64.6). The norites contain 49.8–53.6% SiO_2, 10.2-20.0 wt% MgO, and 9.8–14.8 wt% FeO. Relatively constant SiO_2 content with decreasing MgO and FeO reflects increasing abundance of plagioclase relative to orthopyroxene with progressive fractionation. Likewise, co-variation in CaO (3.0–7.7 wt%, Fig. 3c) and Al_2O_3 (4.9–12.9 wt%) is controlled by the proportion of plagioclase relative to clinopyroxene, orthopyroxene, and olivine. To highlight the differences in mineral abundances, we separate the norites into two groups: high-Ca norites (CaO ≥ 7.5 wt%) and low-Ca norites (CaO < 6 wt%), with a compositional gap from 6 to 7.5 wt% CaO (Fig. 3b). In general, the more differentiated norite samples (high-Ca group) have slightly lower SiO_2 contents, significantly lower MgO and FeO contents, and elevated TiO_2, CaO, Al_2O_3, K_2O, Na_2O as compared to the low-Ca group. ASI varies from 0.57 to 0.72 in the norites but does not clearly correlate with SiO_2.

The sequence of gabbros through monzonites follows a trend of increasing SiO_2, K_2O, and Na_2O contents with decreasing MgO, FeO, CaO, Al_2O_3, and TiO_2 contents (Fig. 3 and S10). ASI gradually increases from 0.70 to 0.96 from the gabbros to the monzonites, in accordance with a decrease in the modal abundance of calcic amphiboles relative to Al-bearing phases. Gabbros are the most voluminous rock type in HLMC and fall into two groups based on major element concentrations: (1) low-SiO_2 gabbros, with 43.9–46.8 wt% SiO_2 and (2) high-SiO_2 gabbros, with 49.2–52.5 wt% SiO_2. The low-Si gabbros have higher proportions of Fe-Ti oxides and pseudomorphic amphiboles relative to clinopyroxenes in the high-SiO_2 gabbros, while high-SiO_2 gabbros contain a greater modal abundance of plagioclase. Al_2O_3 contents are significantly higher in the gabbros (17.3–23.4 wt%) than the norites due to greater abundance of plagioclase and lower abundance of orthopyroxene. The highest Al_2O_3 concentration (23.4 wt%) is at 52.2 wt% SiO_2, then gradually decreases with increasing silica content through the monzodiorites and monzonites.

Two samples from cross-cutting diabase dikes and pods are shown to have very different Mg#s (64.1 and 42.6) despite similar SiO_2 content (47.0 and 49.2 wt%). The lower Mg# sample has considerably higher alkali (Fig. 3a) and

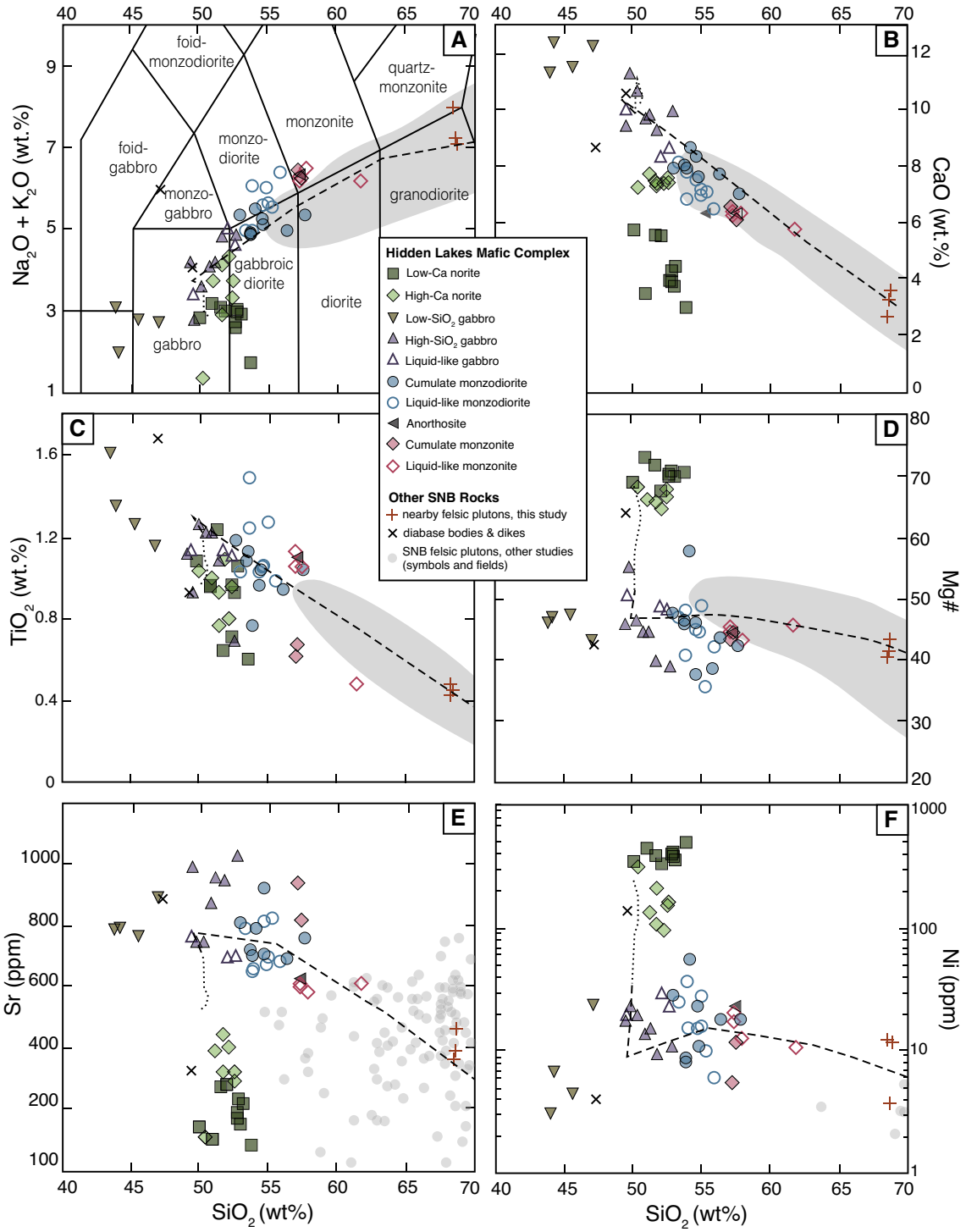

Fig. 3 Bulk-rock major element, trace element, and Mg# vs SiO_2 diagrams for all analyzed HLMC samples. Filled symbols represent samples with cumulate signatures and open symbols represent liquid-like bulk compositions, as defined by criteria discussed in the text and shown in Fig. 5. Plus signs indicate felsic plutons surrounding the HLMC, analyzed in this study. Black dotted and dashed lines show the results of our LLD model. Dotted lines indicate fractionation of lower crustal cumulates and dashed lines trace the upper crustal LLD. The SNB fields in **a**–**d** represent over 800 samples. In the trace element plots (**e**, **f**), SNB compositions are plotted as single points rather than fields, because there are far fewer published analyses available. Note that Ni (panel **f**) is plotted on a log scale. Gray fields and circles define the compositions present in the bulk of the SNB (from the GEOROC database, http://georoc.mpch-mainz.gwdg.de/georoc/)

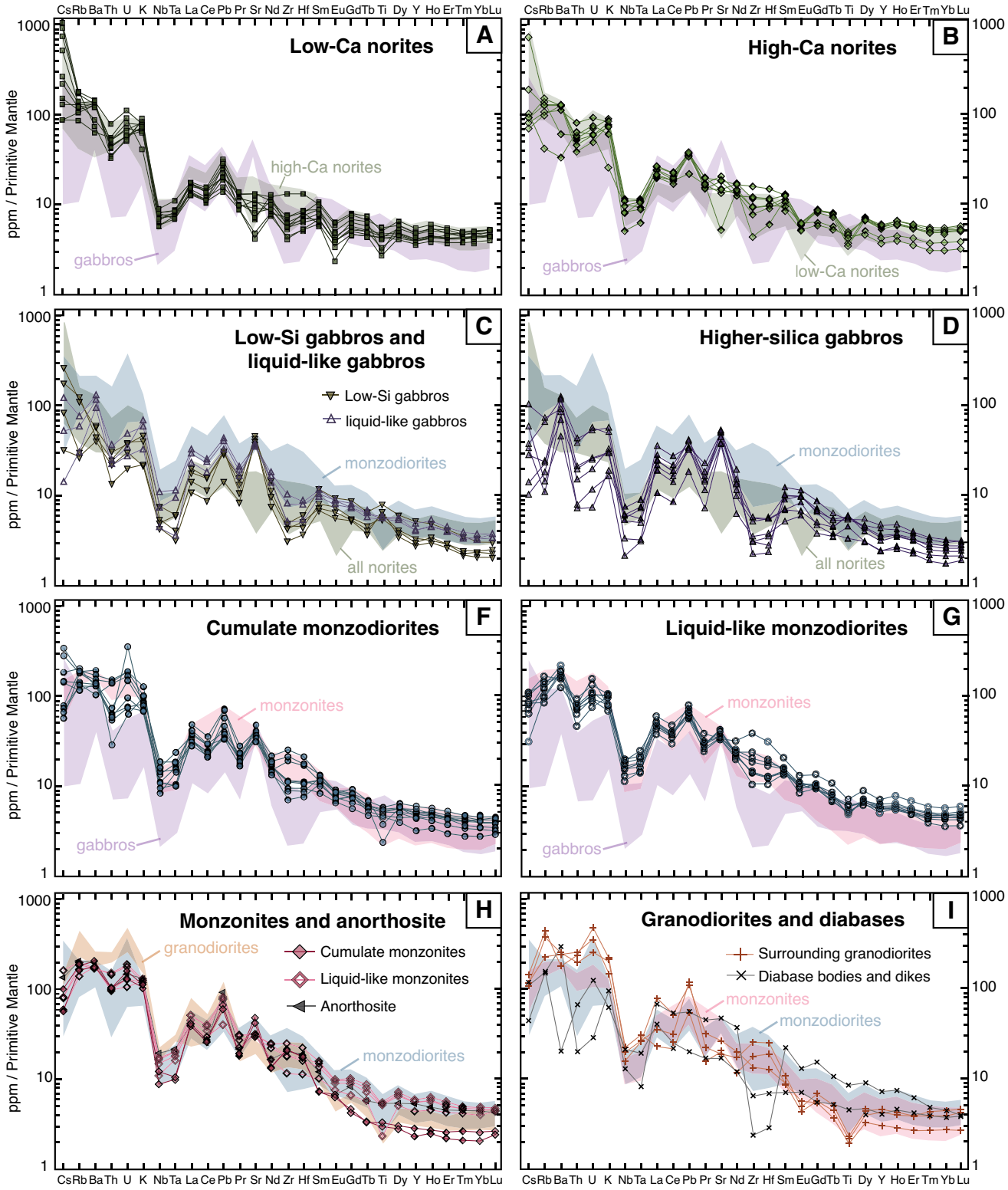

Fig. 4 Bulk-rock trace element compositions for each sample, normalized to the primitive mantle (Sun and McDonough 1989) and separated by lithology. Open symbols represent liquid-like compositions and filled symbols represent cumulates. Shaded fields indicate the range of concentrations within lithologic groups, for comparison. **a** low-Ca norites, **b** high-Ca norites, **c** liquid-like gabbros (purple triangles) and low-SiO_2 gabbros (brown triangles), **d** high-SiO_2 gabbros, **e** cumulate monzodiorites, **f** liquid-like monzodiorites, **g** liquid-like monzonites (pink open diamonds), cumulate monzonites (pink filled diamonds), and anorthosites (gray triangles), and **h** granodiorites (orange plus signs) and diabases (black X's)

P_2O_5 (0.84 wt%) concentrations than other HLMC samples with similar silica contents (~0.25–0.4 wt%), so this sample is unlikely to be cogenetic with HLMC. The higher Mg# diabase is similar in composition to the least primitive norites or highest Mg# gabbros, and therefore may be related to the HLMC system.

Bulk-rock trace element chemistry

Trace element concentrations were collected with solution ICPMS, using acid-digested chips of the glass disks used in XRF analyses. All norite samples have low Sr concentrations (89–407 ppm) that increase with increasing modal abundance of plagioclase (Fig. 3e). Higher Sr contents (705–1030 ppm) in the gabbros are reflective of higher plagioclase abundance. Sr contents in the monzodiorites (659–921 ppm) and monzonites (604–934 ppm) overlap with and extend to slightly lower values compared to the gabbros. Sr/Nd and Al/Si ratios, and Eu anomalies are positively correlated and indicate the extent of plagioclase accumulation. Primitive mantle normalized Eu anomalies ($Eu/Eu^* = Eu_N/sqrt[Sm_N \times Gd_N]$) are < 1 in the norites (0.45–0.78) and 0.72–1.46 in all other HLMC lithologies.

The norites have relatively high Ni and Cr contents (97–504 ppm and 123–551 ppm, respectively, Fig. 3f and S11), which reflect the abundance of orthopyroxene (up to 75%) in these samples, as well as the presence of minor olivine and clinopyroxene. Ni and Cr contents are low in the low-SiO_2 gabbro group (3–24 ppm Ni, 2–21 ppm Cr), then increase slightly, on average, in the high-SiO_2 gabbros and remain relatively constant in the monzodiorites and monzonites.

On primitive-mantle normalized spider diagrams (Fig. 4), all samples display strong Nb and Ta depletions and Pb enrichment consistent with a subduction-related origin for the HLMC parental melts (Miller et al. 1994; Stolz et al. 1996). Most of the gabbros, particularly the low-SiO_2 gabbros, exhibit Ti enrichments as controlled by crystallization of Fe-Ti oxides, biotite, and titanite. Significant titanium depletions are observed in the norites, as these samples lack titanite. Besides the norites, all lithologies display Sr enrichment, reflecting accumulation of plagioclase in higher abundances than olivine and pyroxenes. Some norites are considerably enriched in LIL elements, particularly Cs and Rb (up to 34 and 50 ppm, respectively), likely due to biotite crystallization. In the more evolved rocks and in two norites (Fig. 4a, b, f–i), relative enrichments in Zr and Hf are observed due to the presence of zircon.

Rare-earth elements (REEs) and other incompatible element concentrations (Ba, Th, Nb, Pb, Hf, Ta, U, Rb, Zr) are positively correlated with SiO_2. HREE elements are depleted relative to LREE elements in all rock types, and La/Yb ratios

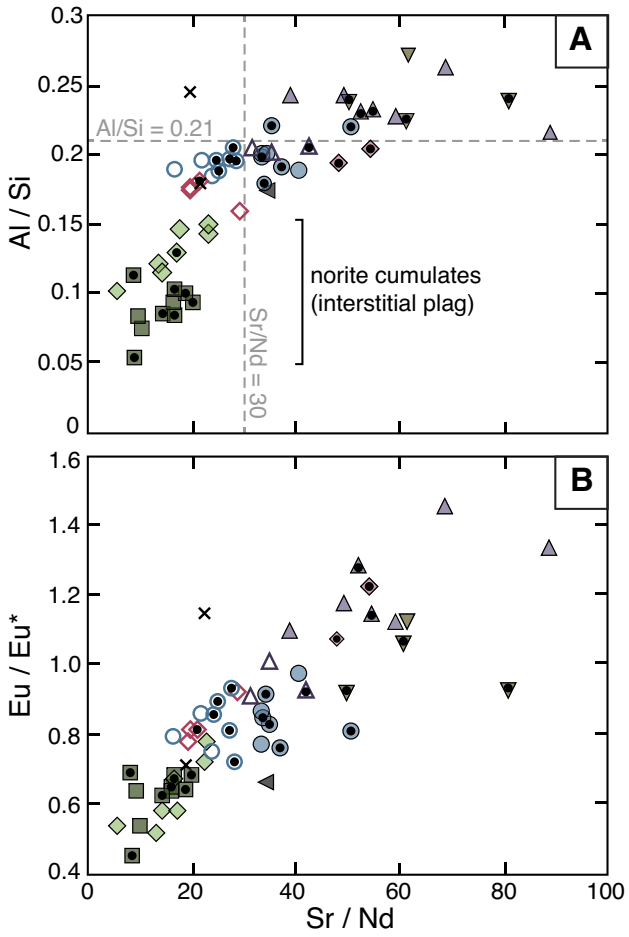

Fig. 5 Bulk-rock major and trace element ratios used to distinguish cumulate and liquid-like samples. Sr/Nd ratio is compared to **a** Al/Si and **b** Eu anomaly, Eu/Eu* (primitive mantle normalized). All ratios indicate the accumulation of plagioclase, which has not significantly occurred in the norites. Symbols represent different rock types and are the same as in Fig. 4. Filled symbols are cumulates and open symbols have liquid-like bulk compositions. The addition of a black circle inside of the symbol indicates petrographic observation of the sample texture

increase with increasing silica content, though there is significant overlap between rock types.

Classification of cumulate and liquid-like samples

Based on textural and compositional parameters, we classify each sample as having a liquid-like or cumulate bulk composition. All norites are classified as cumulates because cumulate textures were identified in all norite thin sections (Fig. 2a), and their bulk-rock Mg#s are significantly higher than the rest of the HLMC (Mg# = 64.6-73.1, with a gap in HLMC from 57.8 to 64.6). Gabbro textures are variable

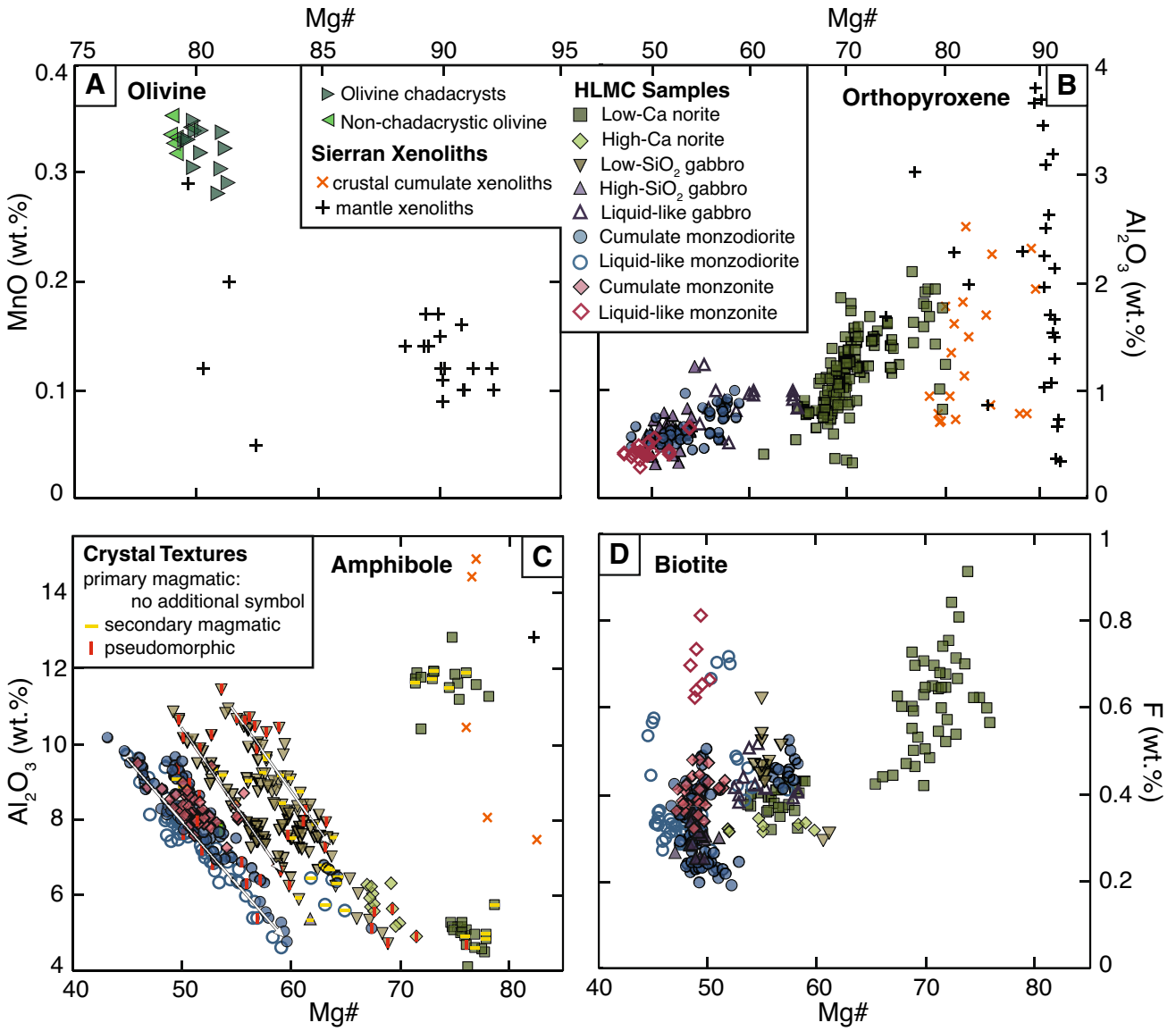

Fig. 6 Selected mineral chemistry, wherein each symbol represents one analysis. **a** MnO in olivine, **b** Al_2O_3 in orthopyroxene, **c** Al_2O_3 in amphibole, and **d** F in biotite. Arrows in c indicate trends caused by subsolidus Tschermak exchange, and additional yellow and red symbols indicate which analyses are from secondary magmatic and pseudomorphic amphibole grains, respectively. HLMC compositions are compared to mantle and lower crustal xenoliths hosted in Neogene volcanic rocks in the Sierra Nevada (Dodge et al. 1986; Dodge et al. 1988; Mukhopadhyay and Manton 1994; Lee et al. 2001, 2006). No biotite analyses from the xenoliths have been reported

from meso- or orthocumulates, to randomly oriented masses of interlocking crystals (Fig. 2d). The latter is suggestive of rapidly crystallized melt-like lithologies. In addition, we use Al/Si and Sr/Nd ratios as tracers of plagioclase accumulation (Jagoutz 2010; Bucholz et al. 2014) and define cumulate gabbros as those with Al/Si > 0.21 and cumulate monzodiorites and monzonites as those with Sr/Nd > 30 (Fig. 5a). These values place samples with textural observations into the correct categories and allows us to classify samples for which we do not have petrographic constraints.

When compared to the macroscopic rock textures, all liquid-like gabbros are medium–fine-grained gabbros, and all coarse-grained and spotted gabbros are cumulates. Some medium–fine-grained gabbros are also classified as cumulates based on our compositional criteria. Eu anomalies are variable within rock types, and either similar between liquids and cumulates of the same rock type (e.g., liquid-like monzodiorites and cumulate monzodiorites) or slightly elevated in the cumulate group. Eu anomalies are < 1 in the norites (0.45–0.69), reflecting minimal plagioclase accumulation

and incompatibility of Eu^{2+} in olivine and orthopyroxene (Fig. 5b).

Mineral chemistry

Major element compositions of minerals were collected using electron probe microanalysis (EPMA) on roughly 3–10 grains per phase in each sample. In zoned crystals, at least 3 points were analyzed in each grain to assess core-to-rim compositional variation. Selected mineral compositions are summarized in Fig. 6, and additional variation diagrams and geochemical data are included in the Supplementary Files (Fig S5-S8, Table S3).

Olivine

Olivine is rare in HLMC and present only in two low-Ca norite samples, SNB-14-62 and SNB-14-52. The highest Mg# olivine analyses are found as chadacrysts within in large amphibole oikocrysts. Olivine chadacrysts have Mg#s ranging from 80 to 81, while non-chadacrystic olivine grains have Mg#s ranging from 79 to 80, while olivines from cumulate xenoliths crystallized in the SNB lower crust extend to Mg# 92 (Dodge et al. 1986; Lee et al. 2001). Olivines have 0.28–0.35 wt% MnO, which is negatively correlated with Mg# (Fig. 6a).

Orthopyroxene

Orthopyroxene is abundant in the norites, occasionally present in the gabbros, and rare in the monzodiorites and monzonites where it is found only in amphibole cores. The Mg# of orthopyroxenes decreases from the norites (65–80) to the gabbros (51–65). In the monzodiorites and monzonites, compositions significantly overlap with those in the gabbros (Mg#=49–59), suggesting that these lithologies experience an early interval of orthopyroxene crystallization followed by amphibole crystallization.

Orthopyroxene Cr_2O_3 contents generally decrease with decreasing Mg# and vary from 0.01 to 0.11 wt% in the norites and are below detection limit to 0.03 wt% in the gabbros, monzodiorites, and monzonites. Similarly, Al_2O_3 is positively correlated with Mg#, ranging from 0.35 to 2.1 wt% in the norites and 0.29 to 1.1 wt% in all other orthopyroxene-bearing lithologies (Fig. 6b). MnO increases with decreasing Mg# and varies between 0.30 and 0.55 wt% in the norites, and 0.59 and 1.1 wt% in the gabbros and monzodiorites. The monzonites have slightly higher orthopyroxene MnO concentrations of 0.95–1.2 wt%.

There is a significant range in orthopyroxene Al_2O_3 contents in the SNB xenoliths (0.7–5.4 wt%; Dodge et al. 1986; Lee et al. 2001), likely due to crystallization at a range of temperatures and pressures. Mg#s of these grains overlap with compositions in the norites and gabbros, as well as extend to higher Mg#s (maximum 92).

Clinopyroxene

Clinopyroxene is a minor phase in the norites (< 5% modal abundance), common in the gabbros, and occasionally present in the cores of amphiboles in the monzodiorites and monzonites. In the norites, clinopyroxene Mg#s range from 73 to 79 and decrease from individual grain cores to rims. Analogous to the orthopyroxenes, clinopyroxene compositions in the gabbros, monzondiorites, and monzonites are very similar to one another. In particular, the clinopyroxenes from the cumulate gabbros and the liquid-like monzondiorites overlap significantly in Mg#, which may indicate that these clinopyroxenes in HLMC may have crystallized from a melt similar to the gabbros. Clinopyroxene Mg#s vary from 61 to 73 in the gabbros, 61 to 75 in the monzodiorites, and 60 to 68 in the monzonites.

Clinopyroxene Cr_2O_3 contents are roughly correlated with Mg#, ranging from 0.03 to 0.11 wt% in the low-Ca norites, 0.02–0.03 wt% in the high-Ca norites, and commonly below detection limit (~0.015 wt%) in all other rock types, with a maximum of 0.04 wt%. Clinopyroxene MnO content increases consistently with decreasing Mg# (from 0.18 to 0.56 wt%). Al_2O_3 content is variable between 0.47 and 2.8 wt%, commonly decreasing (~75% of grains) and occasionally increasing (~25% of grains) from crystal cores to rims. Al_2O_3 in clinopyroxene cores increases from the norites (0.56–1.28 wt%) and peaks at 1.79 wt% in the liquid-like gabbros, then decreases through the gabbros, monzodiorites, and monzonites to 1.09 wt%. This peak corresponds to the maximum in bulk-rock Al_2O_3 concentration.

Amphibole

Amphibole is present in all rock types in HLMC and may be a primary magmatic phase, secondary magmatic overgrowth on pyroxene crystals, or pseudomorphic replacement of pyroxene due to reaction with an evolving melt. There is no distinct compositional difference between these occurrences; however, pseudomorphic amphiboles contain abundant plagioclase micro-inclusions. Amphibole compositions are dominated by magnesiohornblende based on the classification of Leake et al. (1997). Analyses with < 0.75 formula units of Al (calculated on a 23-oxygen basis) are considered metamorphic alteration products and not further discussed. Nearly all amphibole in the high-SiO_2 gabbros (cumulate and liquid-like) is actinolite, while all other rock types contain magmatic amphibole.

There are two compositional populations of amphiboles in the low-Ca norites, which are distinguishable by their aluminum contents and both fall under the classification of magnesiohornblende (Fig. 6c). Mg#s of both groups are comparable, with the high-Al population ranging from 71 to 77 and the lower-Al population ranging from 72 to 79. The high-Al population (9.6–12.8 wt% Al_2O_3) is characterized by primary magmatic oikocrysts that surround olivine grains and is only present in samples SNB-14-52 and SNB-14-62 (*c.f.*, Fig. 2b). This population is also high in TiO_2 (2.9–3.6 wt%) and Na_2O (1.7–2.3 wt%) compared to other amphiboles in the norites with similar Mg#s (0.2–1.3 wt% TiO_2 and 0.6–1.1 wt% Na_2O). The lower-Al population (4.5–5.9 wt% Al_2O_3,) appears to also be of primary magmatic origin based on the euhedral to subhedral crystal shapes. These two populations are not observed in the same samples and so may indicate slight compositional variation between different norite pods. All amphiboles in the high-Ca norites are similar in composition with Mg#s ranging from 67 to 71 and Al_2O_3 varying between 4.8 and 6.3 wt%. Amphibole Mg#s in the gabbros and monzodiorites are negatively correlated with Al_2O_3 in a series of parallel trends, which each represent within-sample compositional variation reflecting subsolidus Tschermak exchange, a trend that is not evident in amphiboles from the norites. Similarly, TiO_2 and Na_2O are negatively correlated with Mg# within individual samples. Amphibole MnO content increases with decreasing Mg# and is relatively constant within each rock type, ranging from 0.09 to 0.31 wt% in the norites, 0.21 to 0.34 wt% in the gabbros, 0.28 to 0.59 wt% in the monzodiorites, and 0.48 to 0.62 wt% in the monzonites. CaO content is negatively correlated with Mg#, though there is considerable overlap between rock types.

Biotite

Biotite is present in all rock types, typically interstitially, and is thus interpreted as a late crystallizing phase. The Mg# of biotite in the low-Ca norites ranges from 54 to 76, with a compositional gap between 59 and 63. The high-Mg# biotite group extends to higher TiO_2 (2.4–5.2 wt%) and F (0.42–0.81 wt%) than the low-Mg# group (1.7–4.1 and 0.32–0.43 wt%, respectively). There is no clear textural difference between the low- and high-Mg# biotite, though individual samples only contain biotite from one compositional group. Biotite Mg# decreases to the high-Ca norites (52–60) and gabbros (47–61). The range of biotite Mg#s in the monzondiorites (45–58) overlaps with that of the gabbros and the monzonites (47–52).

MnO contents systematically increase with decreasing Mg#, from 0.02 to 0.18 wt% in the norites to a maximum of 0.43 wt% in the monzonites. Al_2O_3 content of biotite in the norites is variable (11.9–14 wt%) and not clearly correlated with Mg#. There is significant overlap in Al_2O_3 contents in biotite for the remainder of the studied lithologies (13.2–15.8 wt% in gabbros, 12.9–16.3 wt% in monzondiorites, 12.5–15.6 wt% monzonite). Within individual samples, there is a weak positive correlation between Mg# and Al_2O_3 content of biotite, which is the opposite correlation from what is predicted by Tschermak exchange, and suggests minimal subsolidus alteration. Na_2O contents reach 0.18 wt% in high-Mg# biotite in the norites, and are < 0.11 wt% in other lithologies, and often below detection limit. Fluorine decreases with decreasing Mg#, following established Fe–F avoidance trends (Fig. 6d) (Mason 1992; Icenhower and London 1997). Biotite F content ranges from 0.32

Table 2 Calculated crystallization conditions

	Method	Norites	Gabbros	Monzodiorites	Monzonites
Temperature (°C)	Ca-in-opx[a]	900–1170	930–1100	970–1030	850–1010
	Plag-amph pairs[b]	865–950 (oikocrysts)	740–815 (magmatic amph)	815–870	800–850
		700–765 (non-oikocrystic)	1040–1120 (pseudomorphic amph)		
Pressure (GPa)	Al-in-amph[c]	[0.32][f]	[0.32]	[0.32]	0.32
H_2O (wt%)	Plag hygrometry[d]		2.9–3.5		6–7
fO_2 (ΔNNO, ± 1 log unit)	Biotite[e]				0–0.6

[a]Method of Köhler and Brey (1990)

[b]Method of Blundy and Holland (1990)

[c]Method of Mutch et al. (2016)

[d]Method of Waters and Lange (2015)

[e]Method of Bucholz et al. (2018)

[f]Values in brackets indicate those that were not calculated from that particular rock type due to mineral assemblage constraints, but are assumed to be constant throughout the fractionation sequence (e.g., pressure and fO_2)

to 0.91 wt% in the norites, and in other rock types biotite contains between 0.19 and 0.54 wt% F.

Feldspars

Plagioclase feldspar is dominantly interstitial in the norites, though occasional euhedral crystals are present, and is a common fractionating phase in all other HLMC rock types. The anorthite content (An) of interstitial plagioclase in norites is highly variable, ranging from An_{29} to An_{72}, while euhedral plagioclase has approximately An_{82}. Euhedral to subhedral plagioclase in the gabbros can have distinct core and rim compositions with An_{76} to An_{92} cores and An_{40} to An_{62} rims. In crystals without a core-rim compositional difference, the composition is comparable to the aforementioned rims. Distinct cores and rims are present in < 5% of plagioclase crystals in the monzodiorite plagioclase and absent from the monzonites. Plagioclase is An_{27} to An_{58} in rims and ~ An_{77} in cores in the monzodiorites, and An_{31} to An_{54} in the monzonites.

Alkali feldspar is found as small, interstitial grains in the norites and gabbros, but becomes increasingly common in the monzodiorites and monzonites. Orthoclase (Or) and albite (Ab) content is similar for all rock types, with variation between $Or_{72}Ab_{18}$ and $Or_{98}Ab_{2}$.

Zircon

Zircon grains from HLMC have Ti concentrations ranging from 2 to 24 ppm in the monzonites, 4 to 31 ppm in the anorthosites, and 5 to 27 ppm in the monzodiorites. Zircon is rare in the gabbros and norites and was therefore not separated for analysis. Hf concentration is negatively correlated with Ti concentration within each sample, ranging from 8610 to 17,100 ppm, with 2470 to 7670 ppm of intra-sample variation.

REE concentrations of melts in equilibrium with the zircons were calculated using the methods of Chapman et al. (2016) (Fig S9). Primitive mantle normalized REE (plus Nb and Y) patterns of calculated melts are nearly parallel to the corresponding whole-rock patterns. In cumulate samples, calculated melt compositions are similar to the whole-rock concentrations in the LREE, and slightly higher or lower in the HREE. Calculated melts have Eu anomalies < 1 (0.70–0.81) that are slightly lower or equal within error (2 sigma of all analyses within a sample) than in the corresponding whole-rock composition, implying that zircon saturation occurred after some plagioclase fractionation.

Discussion

Crystallization conditions

Out best estimates for crystallization pressures, temperatures, H_2O content, and fO_2 and of HLMC lithologies are summarized in Table 2 and described below.

Pressure

We perform Al-in-hornblende barometry calculations using amphibole analyses from monzonites, as this is the only HLMC lithology that contains the requisite phase assemblage for this calibration (Mutch et al. 2016). Additionally, these samples exhibit a lesser degree of Tschermak exchange than the gabbros and monzodiorites, a process which could result in inaccurately low calculated pressures. Using high-Al (7.5–8.8 wt% Al_2O_3), low-Mg# (46–56) amphibole analyses (i.e., those inferred to have experienced the least Tschermak exchange) we calculate pressures of 0.30–0.34 GPa. Assuming an average density of 2.8 g/cm^3 for the overlying largely granitic crust (Christensen and Mooney 1995), this equates to an approximate depth between 11 and 13 km.

Temperature

We use a variety of mineral thermometers to constrain crystallization temperatures across the range of HLMC lithologies. For these calculations, we utilize analyses from the rims of adjacent grains to give the best estimate of equilibrium compositions. In the gabbros, orthopyroxene and clinopyroxene pairs are out of Fe–Mg equilibrium, with partition coefficients ($[Fe/Mg]_{cpx}/[Fe/Mg]_{opx}$) of 0.65–0.86 as opposed to the equilibrium value of 1.09 ± 0.14 (Putirka 2008). This is not surprising due to the presence of pervasive exsolution lamellae for samples with coexisting ortho- and clinopyroxene. Thus, two-pyroxene equilibrium temperatures of 760–950 °C (Köhler and Brey 1990; Putirka 2008) likely represent cooling, rather than primary crystallization temperatures. The norites, however, lack discernable pyroxene exsolution and contain little to no clinopyroxene that could react with the available orthopyroxene. Orthopyroxene in the norites has CaO contents ranging from 0.6 to 1.6 wt%, yielding crystallization temperatures of 900–1170 °C based on the Ca-in-orthopyroxene thermometer of Köhler and Brey (1990).

Evidence of subsolidus chemical exchange is found in amphibole analyses in the gabbros, monzondiorites, and monzonites, as intra-sample negative correlation between Mg# and Al_2O_3 in amphibole suggests alteration of the original magmatic compositions by Tschermak exchange (Fig. 6c). However, in the norites, amphibole is present in

two distinct compositional populations that do not define a continuous trend of decreasing Al_2O_3 with increasing Mg#, which we interpret as preserving magmatic amphibole compositions. In the gabbro, monzonite, and monzodiorite samples, we calculate crystallization temperatures based on amphibole compositions with relatively high Al_2O_3 contents (> 7.5 wt%) to avoid sites significantly affected by subsolidus alteration. We do not report crystallization temperature estimates from the pseudomorphic amphibole grains, as these are likely out of equilibrium due to incorporation of excess Ca from the reaction of melt + clinopyroxene → melt + amphibole into the plagioclase needed for temperature calculation.

Thermometry based on the SiO_2 and anorthite contents of coexisting amphibole and plagioclase, respectively, (Blundy and Holland 1990) defines a wide range of crystallization temperatures within HLMC depending on the rock type. As analyses of amphiboles in the norites do not follow a trend of decreasing Al_2O_3 content with increasing Mg# as expected if significant Tschermak exchange has significantly affected the mineral compositions, we believe the estimated temperatures from the norite samples are representative of crystallization conditions. Calculated crystallization temperatures of amphibole oikocrysts and associated plagioclase in the norites are 865–950 °C, using amphibole SiO_2 contents ranging from 40.5 to 42.9 wt% and plagioclase compositions of An_{58} to An_{61}. Estimates from non-oikocrystic amphibole in the same samples are significantly lower, ranging from 700 to 765 °C, using amphibole SiO_2 contents ranging from 46.5 to 50.5 wt% and plagioclase compositions between An_{23} and An_{52}. Locally elevated H_2O contents in some norite pods may have allowed for earlier amphibole saturation in some norites, as the oikocrystic, high-Al amphiboles are not found in all norite samples. The high-Al oikocrysts likely crystallized earlier in the fractionation sequence than the low-Al amphiboles, as they record higher crystallization temperatures and contain inclusions of olivine, which are not found in the low-Al amphiboles. The lack of olivine inclusions in the low-Al amphiboles may indicate that olivine was lost from the fractionating assemblage in favor of orthopyroxene prior to crystallization of the low-Al amphiboles.

In the gabbros, primary and secondary (i.e., rims on pyroxenes) magmatic amphibole temperatures are indistinguishable from one another and range from 740 to 880 °C (SiO_2 in amphibole 44.3–50.6 wt%, anorthite content An_{37-81}). Using the same method, monzodiorites and monzonites yield amphibole-plagioclase crystallization temperatures of 815–870 °C (SiO_2 in amphibole 42.6–48.6 wt%, anorthite content An_{35-52}), and 800–850 °C (SiO_2 in amphibole 41.8–45.2 wt%, anorthite content An_{34-51}), respectively.

Water content and oxygen fugacity

Relatively early crystallization of amphibole, and to a lesser extent biotite, in the HLMC fractionation sequence requires a hydrous parental melt. We apply the plagioclase-liquid hygrometer of Waters and Lange (2015) to plagioclase cores in the liquid-like gabbros to estimate melt H_2O content. Plagioclase core compositions are used because they represent the earliest crystalized sections, which are most likely to be in equilibrium with the bulk-rock "melt" composition. Using 990–1100 °C as the temperature range for the onset of gabbro crystallization in HLMC based on experimental studies at upper crustal pressures and bulk compositions similar to the HLMC gabbros (Grove et al. 2003; Hamada and Fujii 2008), we estimate H_2O contents of 2.9–3.5 wt% in the liquid like gabbros.

Oxygen fugacities (fO_2) play a significant role in the Fe–Mg partitioning into ferromagnesian minerals during crystallization. Oxygen fugacities elevated above that for mid-ocean ridge basalts (near the fayalite-magnetite-quartz buffer) are expected, as arc magmas are commonly characterized by fO_2 at NNO or higher (Sisson et al. 2005; Kelley and Cottrell 2009; Rowe et al. 2009; Brounce et al. 2014). Applying the oxybarometer of Loucks et al. (2020), which utilizes the concentrations of U, Ti, and Ce in zircon grains, we find a range of fO_2 values from ΔNNO − 1.6 to 1.3 in the dated grains from monzodiorite and monzonite samples, with an average fO_2 of ΔNNO − 0.5. We use biotite and bulk-rock compositions and MELTS thermodynamic modeling to calculate fO_2 as presented in Bucholz et al. (2018) for melt-like monzonite SNB-16-9, which contains a relatively narrow range of biotite compositions (Fig. 6d and S6) and thus subsolidus reequilibration was likely minimal. We find that the HLMC melts are oxidized to between NNO and ΔNNO + 0.6 (± 1 log unit).

Comparison to previous studies

Our results from Al-in-hornblende barometry indicate a crystallization pressure of between 0.30 and 0.34 GPa, which is consistent with previous studies and show that the SNB around HLMC crystallized in the upper crust. The central SNB exposes dominantly upper crustal intrusions that crystallized between 0.1 and 0.4 GPa. Previous studies place the location of HLMC at pressures of 0.2–0.3 GPa (Ague and Brimhall 1988; Chapman et al. 2012), and 0.3–0.35 GPa (Nadin et al. 2008).

The following experimental studies were selected for comparison as they produce the series of mineral assemblages observed in HLMC. Our upper temperature estimate for the norites based on the Ca-in-orthopyroxene thermometer (1170 °C) is similar to experiments by Hamada and Fujii (2008), which produce an

olivine + orthopyroxene + plagioclase assemblage from a high-MgO basalt starting at 1160 °C, 0.4 GPa, 1.6–2.7 wt% H_2O, and one log unit above the Ni–NiO buffer (ΔNNO + 1). Clinopyroxene appears in the experimental assemblage at 1130 °C, and the assemblage of orthopyroxene + clinopyroxene + plagioclase + Fe-oxides continues to 1100 °C and the termination of the experiment. The assemblage orthopyroxene + clinopyroxene + plagioclase + amphibole first crystallizes at 990 °C, 0.2 GPa, NNO, and 4.5 wt% H_2O in experiments by Grove et al. (2003). Based on these two studies, which replicate the mineral assemblages found in the norite and gabbro cumulates in HLMC and bracket the pressure and H_2O content estimates for the HLMC and were performed at similar fO_2 conditions, the onset of gabbro fractionation, characterized by common clinopyroxene and minimal orthopyroxene, likely occurred between 1100 and 990 °C.

Experiments by Blatter et al. (2013) using an arc basalt starting material similar to HLMC melt-like gabbro compositions first crystallize amphibole + orthopyroxene + clinopyroxene + plagioclase from a primitive high-Al arc basalt at 0.4 GPa, 1000 °C, and 4 wt% H_2O. However, in these experiments orthopyroxene and clinopyroxene are present in roughly equal proportions and olivine is not present, unlike the HLMC norites. Orthopyroxene is part of the fractionating assemblage of mid-ocean ridge dacites during 0.2 GPa crystallization experiments under oxidizing conditions (NNO + 1 to + 2.1) with H_2O contents between 0.8 and 2 wt% (Erdmann and Koepke 2016). At higher water contents (> 2 wt%) in these experiments, the assemblage lacks orthopyroxene. The dominance of orthopyroxene over clinopyroxene in the first crystallized HLMC cumulates indicates a reduced H_2O content compared to Blatter et al. (2013), but the early crystallization of amphibole suggests H_2O contents higher than in experiments conducted by Erdmann and Koepke (2016) (H_2O > 2 wt%). Experimental evidence thus constrains the H_2O content of the HLMC parental melt between 2 and 4 wt%.

In the HLMC norites, amphibole oikocrysts containing olivine imply that these phases coexist in the magma. Crystallization experiments of Krawczynski et al. (2012) limit the stability of the crystallizing assemblage of olivine + amphibole to between an fO_2 of NNO and ΔNNO + 3 at 0.3 GPa at the calculated crystallization temperature of the oikocrystic amphiboles (~ 950 °C). This study complements our fO_2 calculations in the monzodiorites and monzonites (fO_2 ~ NNO-ΔNNO + 0.6), and shows that the parental melt to HLMC was similarly oxidized in comparison to the more evolved lithologies.

A cogenetic fractionation sequence

Field and petrographic evidence

The western limb of HLMC is composed of mainly medium–fine-grained gabbro with elongate, N–S trending texturally distinct gabbro bodies (coarse-grained and spotted gabbros, Fig. 1). All coarse-grained and spotted gabbros, as well as some of the medium–fine-grained gabbros, exhibit ortho- to mesocumulate textures. The contacts between individual gabbro bodies and the medium–fine-grained gabbro are gradational over 1–5 cm, exhibiting mingling textures and inclusions of gabbros with contrasting textures (Fig S2, S3). These characteristics suggest that the gabbros of the western limb accumulated from multiple pulses of magma that supplied compositionally similar melts within a relatively short period of time, such that previously intruded gabbroic magma was still partially molten to allow for mingled and gradational contacts. Due to their close temporal association, these pulses of magma likely originated from the same source, and are therefore part of a cogenetic sequence. The presence of both liquid-like and cumulate gabbros in the western limb suggest that the parental melts to the gabbros continued to fractionate in situ.

The southeastern section of the HLMC consists of a single large medium–fine-grained gabbro body containing norite and anorthosite cumulate pods, as well as a lens of coarse-grained gabbro, but is overall more texturally homogeneous than the western section. The presence of well-defined cumulate textures in these rocks indicates that separation of crystals and liquid occurred within the mafic complex. The contacts between gabbros, monzodiorite, and monzonite in the northern and northeastern section of the HLMC (Fig. 1) are largely gradational over 5–10 m, and there is no distinct contact between the medium–fine-grained gabbros of the western limb and this lithology in the eastern section. This suggests that eastern HLMC and the western medium–fined-grained gabbros were emplaced as a single large intrusion that differentiated in situ to create the norite and gabbro cumulates and melt was extracted from the gabbros to produce the more evolved monzodiorites and monzonites. This is consistent with petrographic observations suggesting that most of the gabbros are meso- and adcumulates, with the exception of three liquid-like gabbro samples.

The presence of both cumulate and liquid-like gabbros, monzodiorites, and monzonites suggests that the gabbroic HLMC parental intrusions fractionated in situ. Multiple intrusions into the medium–fine-grained gabbro are preserved as gabbros with contrasting textures, and the bodies that represent separate intrusions all have parental melts of similar composition. The gradational boundaries between the gabbros and monzonitic lithologies, as well as evolved pods within the gabbros, indicate that the evolved lithologies

were generated by extraction of melt from the gabbroic cumulates. While some melts may have been extracted to shallower levels in the crust, the liquid-like compositions present in HLMC represent melts generated by fractionation within HLMC.

Evidence for mixing between HLMC and felsic melts at the level of emplacement is minimal and confined to the outer margins of the complex, and so is unlikely to have caused the compositional variation within the mafic body. Locally, the 90.5–96.5 Ma HLMC parental melts intruded into the much older granite of Chickenfoot Lake (Jcf, 191.6 Ma), which would have been fully crystallized prior to the mafic intrusions. Any volume of Jcf-derived felsic melt would need to be produced by heat from HLMC intrusions. This effect is visible along the HLMC-Jcf contact, where a dioritic gradational zone (Fig S3b) indicates short-distance mixing between a HLMC parental melt and granitic melt produced by partial melting of Jcf. However, this hybridized lithology does not extend more than 1 m from the granite–gabbro contact. The contact between Kle and HLMC is sharp and indicates little to no mixing or assimilation. Because Krv is younger than HLMC, and HLMC-sourced blocks in the brecciated contact between these units are angular with sharp contacts, HLMC was likely solidified by the time of Krv intrusion and therefore could not mix. Field evidence precludes substantial magma mixing origin for the compositional diversity within the HLMC and supports in situ fractional crystallization.

Geochemical evidence

The HLMC compositional trends suggest that the various rock types are related to one another by fractional crystallization. Bulk-rock analyses preserve a wide range of SiO_2 contents from 43.6 to 61.5 wt% (Fig. 3). Bulk-rock Mg# decreases from 73.1 to 35.8, though a compositional gap exists between the norites and gabbros (Mg# = 57.8–64.6). Al_2O_3, TiO_2, CaO, MgO, and FeO contents are variable over approximately constant SiO_2 content in the norites, then smoothly decrease from the gabbros to monzodiorites to monzonites. Similar trends are present in K_2O and Na_2O, but their concentrations increase with increasing SiO_2 content. These compositional relationships are consistent with a fractional crystallization liquid line of descent (LLD) and associated cumulates in arc settings (Müntener and Ulmer 2018).

In general, incompatible trace element concentrations in liquid-like samples increase with increasing SiO_2 content, indicating enrichment of these elements in the remaining melt with progressive fractionation. Exceptions to this are Ni and Cr, which are rapidly removed from the melt during norite crystallization, and Sr which decreases with increasing SiO_2 after saturation of significant amounts of plagioclase. HREE elements are depleted relative to LREE elements in all rock types (Fig. 4), and this depletion, indicated by La/Yb ratio, increases with increasing SiO_2 content. Although there is significant overlap in the degree of HREE depletion between rock types, this pattern nevertheless supports a fractional crystallization origin for the HLMC lithologies.

Mineral compositions are also consistent with a cogenetic fractionation sequence. Very similar trends are seen in ortho- and clinopyroxene, in which MnO and Mg# are negatively correlated and higher Mg#s correspond to lithologies crystallized earlier in the fractionation sequence. Cr_2O_3 and Al_2O_3 in orthopyroxene (Fig. 6b) decrease with decreasing Mg# and with increasing bulk-rock SiO_2 content, indicating depletion of these components in the melt with olivine + pyroxene and plagioclase fractionation. Euhedral plagioclase crystals in the norites have very similar An content to the plagioclase cores in the gabbros and monzodiorites, suggesting that these cores crystalized from a melt similar to the norite parental melt and were progressively rimmed by lower-Ca plagioclase as the remaining melt evolved. In biotite, the observed decreasing F (Fig. 6d) and TiO_2 content with decreasing Mg# corresponds to increasing FeO content in the biotite and decreasing crystallization temperature, respectively.

Thus, both the mineral compositions and modal mineralogy of the rocks indicate derivation by fractional crystallization from a common parental melt defined by a lithological progression of norites → gabbros → monzodiorites → monzonites and a mineral crystallization sequence of olivine → orthopyroxene ± amphibole (high-Al) → clinopyroxene + Fe-Ti oxides → plagioclase + amphibole (low-Al) → biotite → K-feldspar → quartz.

Composition of the HLMC parental melt

We define the HLMC parental melt as a representative, initial melt composition that intruded into the upper crust at the location of HLMC and fractionated to produce the range of observed lithologies. Based on our inferred fractionation sequence, olivine is the first phase to crystallize from the parental melt and is our best indicator of its composition. The most primitive analyzed olivine core in HLMC has a Mg# of 81. We calculate the Mg# of the parental melt coexisting with this olivine to be 51, using the olivine-melt distribution coefficient of 0.32 (Blundy et al. 2020; Beattie 1993) and assuming an fO_2 of NNO and thus Fe^{3+}/Fe^{T} ratio of 0.2 (Kress and Carmichael 1991).

Primitive lavas erupted at continental arcs are thought to be representative of sub-arc mantle melts, and span a Mg# range of 67–73 based on a global compilation by Schmidt and Jagoutz (2017). The Mg# of the HLMC parental melt

(51) is significantly lower than these values and therefore does not represent a (non-modified) partial melt of the mantle, but rather one that has experienced prior differentiation at deeper crustal levels. The major and trace element concentrations (Cr, Ni, Rb, Sr, Y, Zr, Nb, Ba, REEs, Hf, Ta, Pb, Th, U) of the HLMC parental melt are determined via fractionation modeling as discussed below, and included in the Supplementary Data File (Table ST5). Although a basaltic dike exists in HLMC that appears to be a potential parental melt composition based on major element concentrations (SNB-14-39), this sample is significantly enriched in incompatible trace elements (particularly Nb, Rb, La, Ce, Lu, Ta, and Th) relative to the liquid-like samples at similar SiO_2 contents. Thus, we infer that this dike is not a parental melt and prefer the calculated parental melt composition.

Evidence for lower crustal crystallization differentiation

Although the SNB is dominated by felsic plutons that crystallized at shallow pressures (generally < 0.5 GPa; Nadin et al. 2016), direct evidence for deep crustal processes is present as ultramafic to mafic Cretaceous xenoliths in Miocene to Pliocene basalts in the central SNB, sourced from 1 to 3 GPa (Lockwood and Bateman 1976; Peselnick et al. 1977; Domenick et al. 1983; Dodge et al. 1986, 1988; Mukhopadhyay 1991; Mukhopadhyay and Manton 1994; Ducea and Saleeby 1996, 1998; Lee et al. 2001, 2006). In addition, southern exposures of the batholith in the Tehachapi Mountains crystallized at pressures between 0.7 and 1.0 GPa (Ross 1985; Sams and Saleeby 1988; Pickett and Saleeby 1993; Lackey et al. 2005; Saleeby et al. 2008; Klein and Jagoutz 2021; Rezeau et al. 2021). Orthopyroxene compositions from lower crustal garnet pyroxenite cumulate xenoliths range from Mg# ~ 80–90 (Fig. 6b; Dodge et al. 1986; Lee et al. 2006). Using the orthopyroxene-melt distribution coefficient of 0.284 (Beattie 1993) and assuming an fO_2 of NNO (as above), the orthopyroxene crystallized from melts ranging from a primitive mantle melt (Mg# = 69) to a fractionated basalt (Mg# = 48). These cumulates therefore record lower crustal differentiation and the generation of low-Mg basalts that are consistent with the HLMC parental melt composition. Additionally, the most primitive HLMC norite orthopyroxene compositions overlap with the least primitive compositions in the xenoliths (Mg# ~ 80), indicating that both cumulates crystallized from similarly fractionated melts.

Likewise, a lower crustal section of the southern SNB is exposed in the Tehachapi Mountains, and exposes depths of up to 30 km (~ 1.0 GPa) (Ague and Brimhall 1988; Pickett and Saleeby 1993). Within the Tehachapi Complex, the Bear Valley Intrusive suite (BVIS, 0.4–1.0 GPa) consists of tonalite, norites, and hornblende gabbros (Klein and

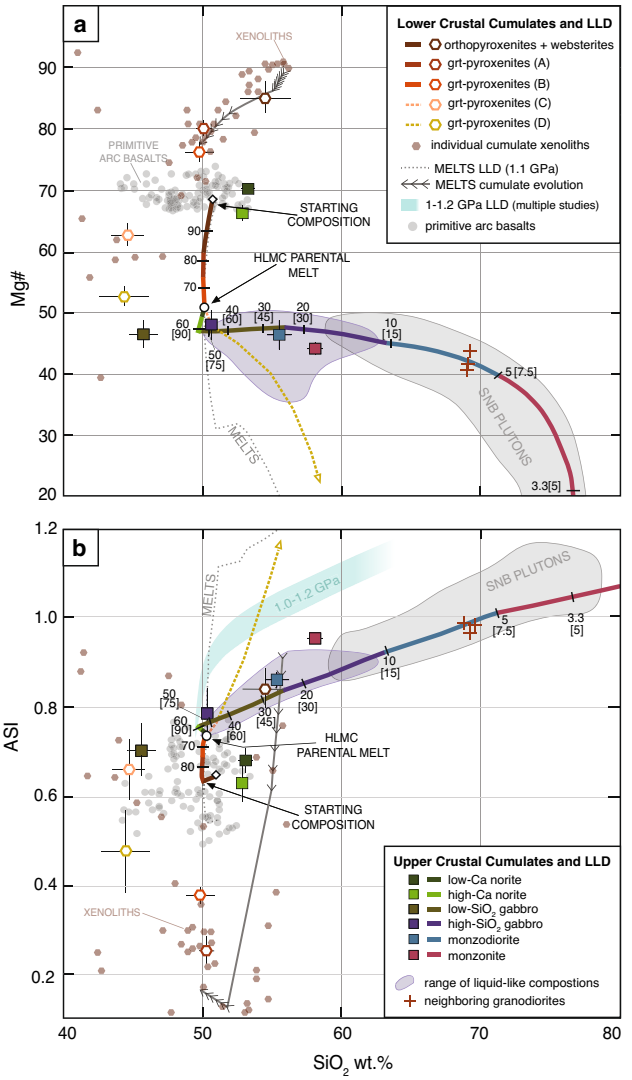

Fig. 7 Summary of LLD modeling, showing **a** Mg# and **b** ASI relative to wt.% SiO_2. Mg# is calculated as Mg/(Mg+Fe) and ASI as Al/(Ca-1.67×P+Na+K). Legends within a and b apply to both panels. Colored squares and open hexagons are the average composition of the cumulate groups in HLMC and xenolith cumulates, respectively, and full compositions are given in Tables S4 and S5. The thick line with colored segments follows crystallization of a primitive arc basalt calculated by incremental subtraction of xenolith (lower crustal) and HLMC cumulate (upper crustal) compositions (Stage 1 and 2 crystallization). Colors of cumulate composition symbols match the line color when that cumulate is crystallizing. Ticks on the LLDs are spaced to show 10% fractionation by mass of the primitive arc basalt and the percent of crystallized mass is labeled at each tick. Numbers in brackets are the % fractionation by mass of the HLMC parental melt during Stage 2. The purple field shows the range of HLMC liquid-like gabbros, monzodiorites, and monzonites. The light blue field in panel b shows the range of arc melt compositions produced at 1-1.2 GPa, as inferred by Blatter et al. (2013) from additional experimental studies (Draper and Johnston 1992; Bartels et al. 1999; Müntener et al. 2001). The dotted gray line is the LLD produced by lower crustal crystallization of a primitive arc basalt at 1.1 GPa and replicating the HLMC parental melt, modeled using alphaMELTS (Ghiorso and Sack 1995; Asimow and Ghiorso 1998). Additional model diagrams are included in the Supplementary Data File

Jagoutz 2021). The mineralogical similarities between the gabbroic cumulate rock types of the BVIS and the HLMC mafic cumulates, particularly the prevalence of amphibole and orthopyroxene, suggest that the melts that intruded into the upper crust are compositionally similar to those that crystallized in the SNB mid-lower crust. Additionally, the most primitive bulk rock analysis of gabbroid cumulates from the BVIS (Mg# = 73.4; Klein and Jagoutz 2021) is similar to the most primitive HLMC norite (Mg# = 73.1), suggesting that the parental melts to both intrusions were similarly evolved basalts. Thus, the parental melts to both the BVIS and the HLMC may be generated by the same process, namely, through deeper crustal differentiation as recorded by the ultramafic xenoliths.

In our case study of HLMC, differentiation of a primitive basalt is required prior to the intrusion of the low-Mg parental melt in the upper crust. We favor lower crustal fractional crystallization over partial melting of underplated basalts as thermal modeling studies demonstrate that this latter process is more likely to produce more silicic rather than basaltic or basaltic-andesite compositions (Annen et al. 2006; Jagoutz and Klein 2018). Remaining possibilities for generating an evolved basaltic melt include assimilation of felsic crust by a primitive basalt or direct fractionation from a primitive basalt in the lower, mid- or upper crust. Assimilation of crustal material is highly unlikely to produce the HLMC parental melt composition from a mantle melt because assimilation of enough crustal melt to decrease the basalt Mg# from ~ 70 to 51 would significantly increase the melt SiO_2 content. Mid- and upper crustal fractionation of large volumes of primitive melts is improbable because ultramafic cumulates are rarely observed at these depths in the SNB. We therefore infer that the initial stage of fractional crystallization occurred in the lower crust within the range of cumulate-dominated lithologies, as observed in accreted arc sections.

Polybaric fractionation model

Field relationships and geochemistry indicate that the HLMC lithologies may be related by a common liquid line of descent (LLD) produced via fractional crystallization, and their trace element signatures indicate that parental melts were likely sourced from a sub-arc mantle melt. However, as discussed above, this parental melt was fractionated relative to a primitive mantle melt. Thus, fractionation must have occurred prior to the intrusion of the HLMC parental melts at their current level in the crust (~ 0.3 GPa) where further differentiation occurred. In agreement with studies of polybaric fractionation in arcs (Almeev et al. 2013; Hamada et al. 2014; Melekhova et al. 2015), we construct a two-stage fractionation model to test our fractional crystallization hypothesis. Stage 1 models fractional crystallization of a primitive mantle melt in the lower arc crust using cumulate compositions of xenoliths crystallized at depths of > 30 km (Lee et al. 2006) to produce a low-MgO basalt that becomes the parental melt to HLMC. Stage 2 tracks fractionation of this evolved basalt in the upper crust by removal of analyzed cumulate compositions from the HLMC from an evolving modeled liquid composition. It is conceivable that multiple episodes of fractionation could have occurred prior to Stage 2 at different levels in the crust below 0.3 GPa. However, we choose the simplest approach and assume only one stage of crystallization prior to intrusion at the level of HLMC exposure. The LLDs generated from our modeling are illustrated in Fig. 7, as well as Figures S10 and S11, and all results of modeling calculations are included in the Supplementary Data File (Tables S4–S6).

Stage 1: Lower crustal fractionation model description

We model the evolution of a sub-arc mantle-derived melt by progressive removal of bulk cumulate compositions from a melt composition, following the methods of Jagoutz (2010). In this initial deep-crustal phase of differentiation, we use representative compositions of cumulate xenoliths (Table S4) that crystallized in the SNB lower crust between 1 and 3 GPa (Dodge et al. 1986; Lee et al. 2006), using a fractionation sequence of orthopyroxenite and websterite → garnet pyroxenite. The starting melt composition was varied within the range of primitive basalts from the Andes, Cascades, Central American, Mexican, and New Zealand continental arcs (Schmidt and Jagoutz 2017). Stage 1 fractionation produces a fractionated melt in equilibrium with the most primitive cumulates in HLMC at the end of the Stage 1 and most successfully reproduces the HLMC liquid-like compositions when input into the Stage 2 model. Stage 1 lower crustal fractionation proceeds until the remaining melt reaches an Mg# of 51 after 33% crystallization, in equilibrium with the most primitive minerals in HLMC.

Because comprehensive trace element concentrations are not available for all xenolith lithologies, we also model Stage 1 fractional crystallization using alphaMELTS (Ghiorso and Sack 1995; Asimow and Ghiorso 1998) to generate a trace element profile for the HLMC parental melt. A crystallization pressure of 1.1 GPa, or ~ 35 km depth, was used to replicate the lower crust of the Sierra Nevada arc as predicted by seismic studies (Jones and Phinney 1998; Ruppert et al. 1998; Fliedner et al. 2000). Following our best estimates for oxygen fugacity, we performed models at NNO. Initial water contents were assumed to be 2 wt% H_2O, which is within the range of primitive (Mg# = 65–74) melt inclusion concentrations from basalts in the Mexican, Cascade, and Kamchatkan arcs (1.0–5.2 wt% H_2O; Sisson and Layne 1993; Cervantes

and Wallace 2003; Portnyagin et al. 2007) and reproduces the H_2O content (2.9–3.5 wt%) of the HLMC gabbros after completion of Stage 1 crystallization. Although the xenolith-based and alphaMELTS models produce the HLMC parental melt composition from slightly different primitive starting compositions and diverge after the melt reaches the HLMC parental melt composition, the orthopyroxenite and clinopyroxenite cumulates produced by the MELTS model are consistent with xenolith compositions from the SNB lower crust (Fig. 7). After generation of the HLMC parental melt, we extend both the xenolith fractionation and MELTS models to Mg# < 51 to assess the melt evolution had it not been extracted from the lower crust (shown as dashed lines in Fig. 7), but this is not included in our polybaric crystallization model.

Stage 2: Upper crustal fractionation model description

We use a similar stepwise cumulate subtraction approach to model the LLD of the HLMC parental melt as it fractionally crystallizes in the upper crust. Average cumulate compositions are calculated for 6 representative lithologies from HLMC (Table S5) following the fractionation sequence discussed above. The starting liquid composition is the HLMC parental melt as generated by our lower crustal fractionation model. We do not use alphaMELTS to model this stage for two reasons: (1) amphibole is a common fractionating phase in the HLMC and alphaMELTS currently lacks an amphibole model that accurately reproduces observed phase assemblages from experimental and natural studies, and (2) the fractionating assemblage and cumulate compositions can be constrained from field and geochemical observations.

Proportions of cumulates crystallized

Cumulate assemblages are introduced to the fractionation sequence based on the calculated Mg# of melts in equilibrium with orthopyroxene and clinopyroxene in the lower-crustal xenoliths, determined using mineral-melt Mg–Fe distribution coefficients of 0.284 and 0.23, respectively (Beattie 1993; Sisson and Grove 1993). Because the garnet pyroxenite xenoliths span a significant range in bulk-rock Mg# (39–83), we split this lithology into four fractionating cumulate groups to more accurately replicate crystallization from an evolving melt: group A (Mg# 80.5–83), group B (Mg# 74–80), group C (Mg# 62–68), and group D (Mg# 39–59). Compositions of cumulates used in this model are averages for each group, and are included in the Supplementary Data File. Fractionation of a primitive arc basalt during Stage 1 fractionation of lower crustal cumulates produces 16.6% (by mass) of orthopyroxenite (±clinopyroxene), 10.2% of group A garnet pyroxenites, 7.0% of group B garnet pyroxenites, and 0.6% of group C garnet pyroxenites. At this point, the melt reaches an Mg# of 51 and ascends into the upper crust where the HLMC cumulates begin to crystallize. Stage 1 differentiation results in 33% total crystallization of cumulates (by mass), closely replicated by 33% crystallization of pyroxenites produced in the alphaMELTS model. The resulting liquid composition is input into the Stage 2 model as the HLMC parental melt.

In accordance with our inferred fractionation sequence, low-Ca norites are the first cumulates to crystallize in Stage 2 (3% crystallization of the remaining melt mass), followed by high-Ca norite fractionation (9.3%), and low-SiO_2 gabbro crystallization (53%). As clino- and orthopyroxenes are consistently exsolved in the gabbros, they are unlikely to record the equilibrium melt composition, and we therefore infer that the Mg# of the melt was between that of the low-SiO_2 (Mg# = 46) and liquid-like gabbros (Mg# = 49) at the onset of high-SiO_2 gabbro crystallization. High-SiO_2 gabbro is assumed to crystallize until the liquid-like monzonite compositions are replicated at 63 wt% SiO_2 (20% crystallization by mass). Fractionation of cumulate monzodiorites continues from 63 wt% SiO_2 and Mg# 44.7 to 70 wt% SiO_2 and Mg# 40 (7.3% by mass). Cumulate monzonites then fractionate until SiO_2 reaches 78 wt% (2.9% by mass), near the maximum for granites in the SNB.

Model results

Our polybaric fractionation model reproduces the range of major and trace element compositions of the HLMC, and when extended to higher SiO_2 contents is capable of replicating the compositional trends defined by the SNB felsic plutons (63–78 wt% SiO_2, Fig. 7). In Stage 1, differentiated melts in equilibrium with the most primitive HLMC minerals are produced by 33% fractionation by mass of a primitive arc basalt at pressures between 1 and 3 GPa (> 30 km). The resulting melt composition is the HLMC parental melt, which has an H_2O content of 3.3 wt% consistent with our estimates from plagioclase hygrometry in the liquid-like gabbros. During this crystallization stage, the Mg# of the melt drops from 68 to 51 with little change in SiO_2 (49.9–48.9 wt%) due to significant fractionation of orthopyroxene and clinopyroxene, with lesser contributions from garnet. Initially, 16.6% by mass of orthopyroxenite (with minor websterite) crystallizes, causing a decrease in Mg# from 68 to 59 (Fig. 7a). Over this interval, MgO in the remaining melt decreases from 11.8 to 8.4 wt%, while all other major oxides increase accordingly and ASI remains stable at 0.64. Garnet pyroxenites (group A, Mg# 80.5–83) begin to fractionate at a melt Mg# of 59, in equilibrium with the highest Mg# clinopyroxene (Mg# = 65, Fe–Mg distribution coefficient 0.23; Sisson and Grove 1993). 10.2% of the melt crystallizes to form group A garnet pyroxenites, causing an increase in melt

ASI from 0.64 to 0.71 and decrease in Mg# from 59 to 55. Following, 6.3% resulting in a melt Mg# of 51 and ASI of 0.74. At this point, the melt is in equilibrium with the most primitive HLMC minerals. If the melt were to remain in the lower crust, the group C and D garnet pyroxenites would proceed to crystallize, causing ASI to further increase, as is described below. Within Stage 1 crystallization, the MgO content of the melt decreases from 11 to 6.2 wt% with a

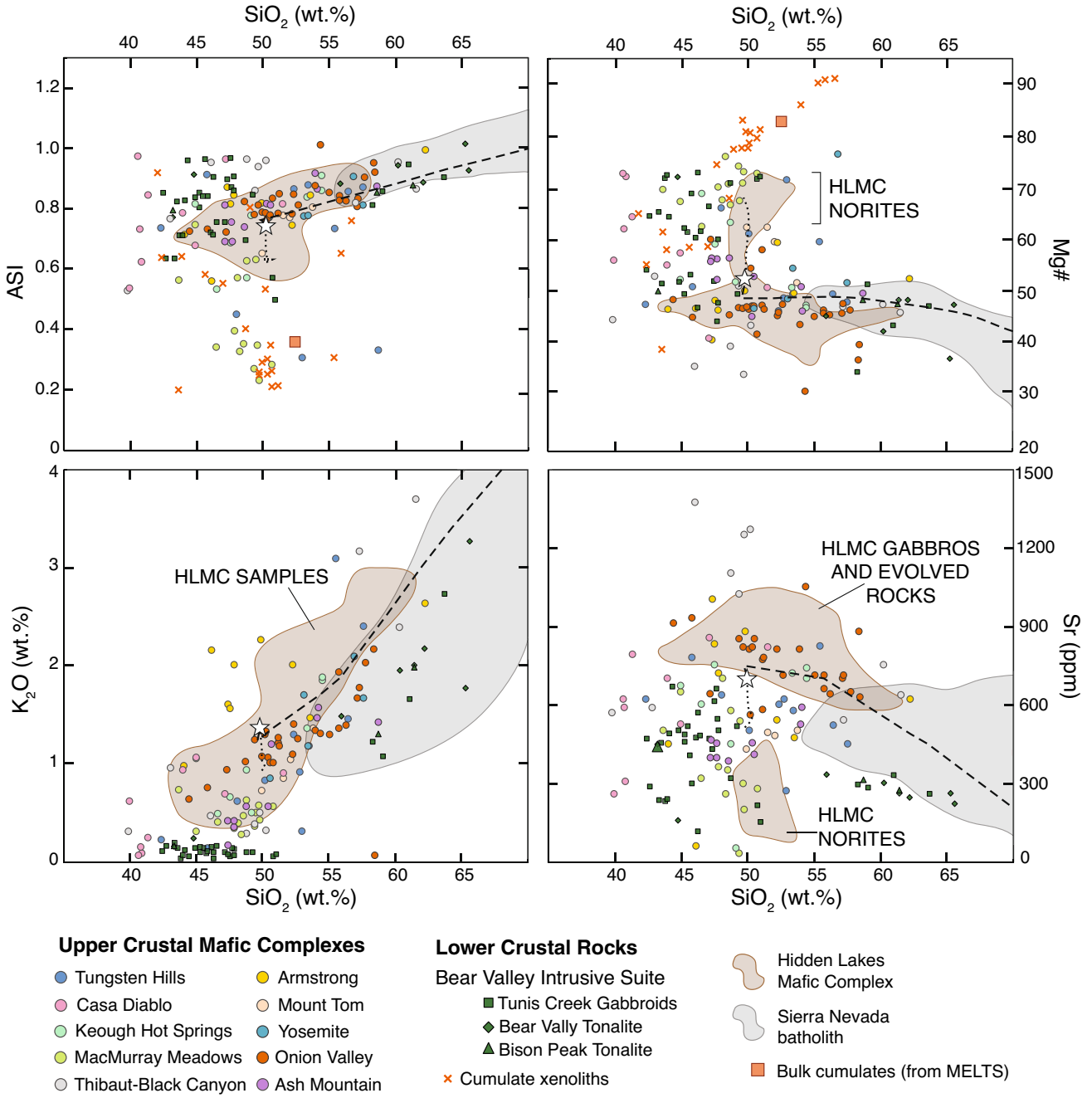

Fig. 8 Bulk-rock compositions from other mafic complexes in the SNB upper crust (Frost 1987; Frost and Mahood 1987; Sisson et al. 1996; Ratajeski et al. 2001; Holland et al. 2013), the lower crustal Bear Valley Intrusive Suite (Klein and Jagoutz 2021), and lower crustal xenoliths (Dodge et al. 1986; Dodge et al. 1988; Lee et al. 2006). Showing **a** ASI, **b** Mg#, **c** K_2O, and **d** Sr, relative to SiO_2. The star denotes the HLMC parental melt composition used in our LLD model. The brown fields encompass all HLMC samples, including both cumulate and liquid-like compositions. The dotted line represents our modeled lower crustal LLD and the dashed line is the upper crustal LLD. Xenolith K2O and Sr contents are commonly below detection limit or not measured, and thus excluded. Gray fields are felsic compositions from the SNB upper crust, attained from the GEOROC database (http://georoc.mpch-mainz.gwdg.de/georoc/)

concurrent increase in FeO from 10 to 10.6 wt%. This crystallization also causes a significant increase in Al_2O_3 from 13.5 to 17.2 wt% with only a slight increase in CaO (9.4–10 wt%), driving the observed rise in ASI.

The derivative basalt produced at the end of Stage 1 is assumed to subsequently ascend, intrude into the upper crust, and further differentiate. The removal of norite cumulates, dominated by orthopyroxene with minor olivine and plagioclase, drives an initial decrease in the melt Mg# from 51 to 47 at relatively steady SiO_2. CaO, Al_2O_3, Na_2O, and Sr contents increase in the melt during this interval due to the paucity of accumulated feldspar in the norites.

Following the onset of low-SiO_2 gabbro crystallization, MgO, CaO, FeO, and TiO_2 smoothly decrease through the remaining LLD, while K_2O, ASI, and incompatible trace elements consistently increase. Fractionation of the low-SiO_2 gabbros causes a significant increase in the melt SiO_2 content from 49.9 to 56 wt%. The low SiO_2 (43.9–46.8 wt%) and high FeO and TiO_2 (9.6–13.6 and 1.2–1.6 wt%, respectively) content of the low-SiO_2 gabbros is due to abundant amphibole and Fe-Ti oxides. As such, fractionation of these cumulates drives the SiO_2 enrichment and FeO and TiO_2 decrease in the melt. The liquid also decreases in MgO and CaO content over this fractionation interval. In contrast to norite fractionation, plagioclase is now a major fractionating phase and the Al_2O_3 content of the melt increases only slightly during low-SiO_2 gabbro fractionation, from 18.2 to 18.5 wt%. Na_2O and P_2O_5 increase due to crystallization of high-Ca plagioclase (~ An_{80}) and a lack of apatite in the low-SiO_2 gabbros.

High-SiO_2 gabbro fractionation continues the trend of increasing SiO_2 content (56–63 wt%) with a limited decrease in Mg# (47–45). Plagioclase is abundant in these cumulates and has lower An content (~ An_{50}) than in the low-SiO_2 gabbros, causing Al_2O_3 to decrease and the rate of Na_2O increase to shallow. Al_2O_3, Na_2O, and P_2O_5 contents continue to decrease for the remainder for the LLD. When gabbro fractionation ceases, the model has reproduced the most fractionated liquid-like monzonite in HLMC with 16.2% of the mass of HLMC parental melt remaining, or 10.9% for the primitive arc basalt.

Fractionation of monzodiorite cumulates from the remaining melt continues the increasing trends in SiO_2 (63–71 wt%), K_2O (3.0–4.5 wt%), and Na_2O (3.5–3.7 wt%). The melt Mg# decreases from 45 to 40, along with decreasing MgO, TiO_2, and FeO primarily due to amphibole and biotite crystallization, and decreasing CaO and Al_2O_3 which are depleted by plagioclase and amphibole fractionation. This crystallization interval replicates a representative SNB granodiorite composition (67.5 wt% SiO_2, Table S5) with 9.9% of the parental melt and 6.6% of the primitive melt masses remaining. Monzonite fractionation continues the monzodiorite fractionation trends, causing the evolving melt composition to increase from 71 to 75 wt% SiO_2. Mg# notably decreases from 40 to nearly 0 as MgO is consumed by fractionating amphibole and biotite. At this point, the remaining granitic melt mass is 5.8% of the HLMC parental melt and 3.9% of the primitive arc basalt.

To determine if the HLMC evolved rocks and SNB granodiorites could be produced by continued lower crustal fractionation, we extend both the lower crustal (xenolith) crystallization model and the alphaMELTS model to Mg#s < 51 (Fig. 7). Although the starting compositions we use are within the low range of Al_2O_3 values found in primitive arc basalts (< 13.5 wt% Al_2O_3) (Schmidt and Jagoutz 2017), our models of lower crustal fractionation always produce peraluminous andesite liquids (i.e., ASI > 1.1 when SiO_2 < 57 wt%). In our model and in the Blatter et al. (2013) experiments, plagioclase does not become a significant fractionating phase at > 0.9 GPa until 33–30% of the initial melt mass is remaining. In the xenolith cumulate crystallization model, Al is initially removal from the melt by minor incorporation into orthopyroxene and has little effect on ASI. Garnet is included in the fractionating cumulates after 17% crystallization, but the group A and B garnet pyroxenites have low Al_2O_3 contents (7.6–8.8 wt%) relative to CaO (12.1–15.7 wt%), leading to a continuous increase in ASI. Thus, the HLMC compositions and non-peraluminous evolved arc melts are inconsistent with extensive lower crustal fractionation.

Comparison to other upper crustal mafic bodies in the SNB

Numerous mafic bodies are preserved in the SNB upper crust and several have been investigated for geochronology and geochemistry (Frost 1987; Frost and Mahood 1987; Coleman et al 1995; Sisson et al. 1996; Ratajeski et al. 2001; Holland et al. 2013). The Onion Valley (92.1 ± 0.3 Ma), Armstrong Canyon (91.5 ± 0.1 Ma), and Lake Sabrina (91.1 ± 0.3 Ma) mafic complexes in the eastern Sierra Nevada (Coleman et al. 1995) are broadly coeval with HLMC (90.5–96.5 Ma). Mafic magmatism in all four localities was contemporaneous with voluminous late Cretaceous felsic intrusions throughout the Sierra Nevada arc (Ducea 2001), demonstrating that mafic and felsic magmatism was coeval and possibly cogenetic.

Geochemical data from the lower crustal Bear Valley Intrusive Suite (Klein and Jagoutz 2021) and 10 upper crustal SNB mafic complexes in addition to HLMC are presented in Fig. 8. All localities are in the eastern SNB from Frost (1987) and Sisson et al. (1996) except for the Yosemite samples of Ratajeski et al. (2001) and the Ash Mountain complex of Holland et al. (2013). Amphibole-gabbros (± olivine) and amphibole-bearing diorites are common throughout the

mafic complexes, indicative of crystallization from hydrous parental melts. In particular, the parental melt to the Onion Valley complex is estimated to have 6 wt% H_2O (Sisson et al. 1996). The most primitive cumulates in the Onion Valley complex are olivine-hornblendites and the intrusion is generally pyroxene poor. This is in contrast to the orthopyroxene-dominated norites of HLMC, which indicates crystallization from a less hydrous parental melt (estimated 3.1 wt% H_2O). In both cases, elevated water contents likely facilitate the ascent of the low-Mg, high-Al basalts into the upper crust due to their decreased density and viscosity (Sisson et al. 1996).

Layered cumulates and internal compositional ranges from gabbro to diorite within each body (Frost 1987; Sisson et al. 1996; McCarthy and Müntener 2016) suggest that in situ upper crustal fractionation is common in upper crustal mafic complexes. Olivines from the Onion Valley complex have a maximum Mg# of 81.7 (in equilibrium with melt Mg# = 52), and sheeted sills interpreted as representative of melt compositions have Mg#s ranging from 41 to 54.5 (Sisson et al. 1996). The most primitive sill and the olivine-melt estimates are slightly more primitive, but still comparable to the HLMC parental melt (Mg# = 51), suggesting that the parental melts to these two bodies were fractionated to a similar degree in the lower crust prior to ascent. Mineral chemistry only exists for the Onion Valley and Hidden Lakes mafic complexes, rendering it is difficult to calculate the Mg# of parental melts for the other complexes. However, maximum bulk-rock Mg#s in each complex range from 53 to 76.5, and therefore did not fractionate from a primitive basalt (Mg# of cumulates > 80). Thus, lower crustal differentiation is required to generate low-Mg basalts in order to produce these upper crustal mafic intrusions. Derivation of the upper crustal mafic complexes from evolved basalts and the presence of upper crustal cumulate lithologies demonstrate that polybaric fractionation is a common process in generating the range of compositions in SNB mafic complexes.

All mafic complex samples have ASI values less than 1, indicating that the mafic melts that escape the lower crust are generally not peraluminous. Samples with high ASI relative to their SiO_2 content (ASI = ~0.8–0.97, SiO_2 = 40.7–50.3 wt%) are likely cumulates, and thus reflect plagioclase accumulation rather than parental melts with initially high ASI values. Lower crustal fractionation of a primitive arc basalt creates peraluminous melts at 51 wt% SiO_2 (our model) to 56 wt% SiO_2 (Blatter et al. 2013) by ~55% crystallization. Thus, melts that generate the mafic complexes must escape the lower crust (> 0.7 GPa) before evolving to andesitic compositions. Because some lithologies found in these complexes have SiO_2 > 56 wt%, upper crustal differentiation must occur to create these compositions after extraction from the lower crust.

Although mineral compositional data is limited to two complexes, those that do exist define a narrow range of parental melt compositions (Mg# = 51–54.5). The range of bulk-rock cumulate compositions from other complexes are similar in Mg# to the Onion Valley and Hidden Lakes mafic complexes, suggesting that all upper crustal mafic complexes may be derived from melts that are fractionated to a similar degree in the lower crust. Additionally, the SiO_2 content of hydrous parental melts cannot exceed 56 wt% without becoming peraluminous during fractional crystallization at > 0.7 GPa. Therefore, we suggest that there may be a narrow window of rheologic properties that allow these hydrous basalts to ascend. For example, the hydrous, but still relatively low-SiO_2 nature of these basalts reduces their viscosity and decreases their density, enhancing their ability to ascend via diking (Sisson et al. 1996).

Production of Sierra Nevada Batholith Granitoids

Our polybaric fractionation model results support the hypothesis that the HLMC is an example of upper crustal fractional crystallization of a low-Mg basalt in a continental arc and that lower crustal fractionation is required to produce the HLMC parental basalt. We show that arc-like granodiorite and granite compositions can be generated by this two-stage crystallization process, and thus, polybaric crystallization can contribute to the generation of non-peraluminous granitoids in the SNB. However, volumes of mafic (noritic to gabbroic) cumulates at upper crustal depths (0.1–0.4 GPa) are relatively small. We posit that the fractionation of a low-MgO basalt deeper than the exposures of much of the SNB, yet at depths sufficiently low to allow for plagioclase saturation (< 0.7 GPa), could generate evolved non-peraluminous melts. Crystallization of "damp" basalt to andesites and enhancement of orthopyroxene stability could also contribute to limiting the increase in ASI of differentiating melts at high pressures (Rezeau et al. 2021). This is supported by gabbro and gabbronorite lithologies with a maximum Mg# identical to the HLMC (Mg# = 73) in the ~0.8–0.9 GPa section of the Bear Valley Intrusive Suite (BVIS; Klein and Jagoutz 2021). Because the BVIS lithologies did not crystallize from a primitive mantle melt, an initial stage of fractionation is required below ~1 GPa, analogous to Stage 1 in our model for the HLMC. Throughout the batholith, Stage 2 fractionation may occur below exposures of the bulk of the SNB (> 0.4 GPa) to produce granodioritic melts consistent with SNB compositions, which proceed to intrude into the upper crust. This reconciles the discrepancy between experimental and observational data, in which experiments indicate that melts produced by lower crustal fractionation rapidly become peraluminous (Cawthorn and Brown 1976; Cawthorn and O'Hara 1976; Blatter et al. 2013; Nandedkar et al. 2014; Müntener and Ulmer 2018; Ulmer et al. 2018),

yet lower crustal ultramafic cumulates are ubiquitous in arc crustal cross sections (Debari and Sleep 1991; Greene et al. 2006; Otamendi et al. 2012; Jagoutz 2014; Walker et al. 2015; Guo et al. 2020). HLMC has captured a local example of upper crustal differentiation, indicating that granodiorite compositions consistent with the SNB can be produced by a polybaric fractionation processes with a range of possible depths for fractionation of a low-MgO basalt.

The volumes of intermediate to evolved (> 60 wt% SiO_2) melt produced by fractional crystallization will be small compared to the volumes of cumulates, so polybaric crystallization may not be the only mechanism for the generation of arc granodiorites. Previously proposed mixing models for the SNB (e.g., Reid et al. 1983; Frost and Mahood 1987; Sisson et al. 1996), require both a high-SiO_2 melt, and an evolved basalt similar to the HLMC parental melt. Although the mechanical viability of mixing felsic and mafic melts is limited, these models also resolve the problem of peraluminous melt compositions generated by lower crustal fractionation, because the homogenized products between non-peraluminous, low-Mg basalts, and mildly peraluminous (i.e., ASI < 1.1) granitic melts are consistent with batholith granitoid compositions (Blatter et al. 2013). Our modeling identifies a potential low-Mg basaltic end member composition (the HLMC parental melt) produced by lower crustal fractionation. We show that evolved basalts must be generated in the lower crust, and are thus available to participate in both mixing and polybaric crystallization processes that contribute to the production of batholith-scale volumes of granodiorite.

Conclusions

The Late Cretaceous Hidden Lakes mafic complex is a preserved example of intrusion of melt into the upper crust of the Sierra Nevada batholith contemporaneously with more voluminous felsic magmas. Bulk compositions of lithologies ranging from olivine norites to monzonites are consistent with fractional crystallization from a moderately hydrous basalt (2.9–3.5 wt% H_2O) at ~ 0.3 GPa, and oxidizing conditions (~ NNO). The parental melt to the HLMC is a low-Mg basalt produced through differentiation in the lower crust prior to intruding into the upper crust.

We model this polybaric fractional crystallization process in two stages, using cumulate compositions from SNB deep crustal xenoliths, accompanied by alphaMELTS, to calculate the composition of an evolving primitive arc basalt in the lower crust (Stage 1) and constructing an upper crustal fractionation based on measured cumulate and liquid-like sample compositions (Stage 2). Our model indicates 33% mass fractionation in the lower crust, followed by extraction to upper crustal pressures and subsequent fractionation to form all HLMC cumulates and melt compositions. Polybaric fractionation of mantle-derived basalt to produce granodiorite resolves the disagreement between the prevalence of lower crustal cumulates in arcs and experimental data that suggest lower crustal fractionation will produce peraluminous melts inconsistent with arc batholith compositions.

The HLMC contains rock types that are lithologically and compositionally similar to those other upper crustal mafic complexes of the SNB, suggesting that these intrusions crystallized from hydrous, fractionated basalts of comparable compositions. Consequently, their composition may be governed by unifying rheologic characteristics that facilitate their ascent from the lower crust, such as reduced density and viscosity.

Supplementary Information The online version contains supplementary material available at https://doi.org/10.1007/s00410-021-01844-y.

Acknowledgements We thank Joe Biasi, Allyson Trussel, and Ben Klein for their assistance in the field, and thank Chi Ma for help with microprobe analyses and Nathan Dalleska for ICPMS support. We are grateful to the UCSB Petrochronology lab and Arizona Laserchron Center for their assistance with zircon LA-ICPMS. The geochronology analyses were supported by Awards for Geochronology Student Research2 funding (via National Science Foundation Grant no. EAR-1322032) awarded to M.J.L. O.J. and C.E.B. were supourted in part by EAR-1322032. Reviews by Cin-Ty Lee and Saskia Erdmann, as well as comments from editor Othmar Müntener, have been very helpful for improving this manuscript and are greatly appreciated.

References

Ague JJ, Brimhall GH (1988) Magmatic arc asymmetry and distribution of anomalous plutonic belts in the batholiths of California: effects of assimilation, crustal thickness, and depth of crystallization. Geol Soc Am Bull 100(6):912–927

Almeev RR, Ariskin AA, Kimura J-I, Barmina GS (2013) The role of polybaric crystallization in genesis of andesitic magmas: phase equilibria simulations of the Bezymianny volcanic subseries. J Volcanol Geoth Res 263:182–192

Annen C, Blundy J, Sparks R (2006) The genesis of intermediate and silicic magmas in deep crustal hot zones. J Petrol 47(3):505–539

Arai S, Ishimaru S (2008) Insights into petrological characteristics of the lithosphere of mantle wedge beneath arcs through peridotite xenoliths: a review. J Petrol 49(4):665–695

Asimow PD, Ghiorso MS (1998) Algorithmic modifications extending MELTS to calculate subsolidus phase relations. Am Miner 83(9–10):1127–1132

Bartels KS, Kinzler RJ, Grove TL (1991) High pressure phase relations of primitive high-alumina basalts from Medicine Lake volcano, northern California. Contrib Miner Petrol 108(3):253–270

Bas ML, Maitre RL, Streckeisen A, Zanettin B, Rocks ISotSoI (1986) A chemical classification of volcanic rocks based on the total alkali-silica diagram. J Petrol 27(3):745–750

Bateman PC (1992) Pre-Tertiary bedrock geologic map of the Mariposa 1° by 2° quadrangle, Sierra Nevada, California; Nevada. The Survey

Bateman PC, Eaton JP (1967) Sierra Nevada Batholith: the batholith was generated within a synclinorium. Science 158(3807):1407–1417

Beattie P (1993) Olivine-melt and orthopyroxene-melt equilibria. Contrib Miner Petrol 115(1):103–111

Blatter DL, Sisson TW, Hankins WB (2013) Crystallization of oxidized, moderately hydrous arc basalt at mid-to lower-crustal pressures: implications for andesite genesis. Contrib Miner Petrol 166(3):861–886

Blundy JD, Holland TJ (1990) Calcic amphibole equilibria and a new amphibole-plagioclase geothermometer. Contrib Miner Petrol 104(2):208–224

Blundy J, Melekhova E, Ziberna L, Humphreys MC, Cerantola V, Brooker RA, McCammon CA, Pichavant M, Ulmer P (2020) Effect of redox on Fe–Mg–Mn exchange between olivine and melt and an oxybarometer for basalts. Contrib Miner Petrol 175(11):1–32

Brounce M, Kelley K, Cottrell E (2014) Variations in Fe3+/$\sum$ Fe of Mariana Arc basalts and mantle wedge fO2. J Petrol 55(12):2513–2536

Bucholz CE, Spencer CJ (2019) Strongly peraluminous granites across the Archean-Proterozoic transition. J Petrol 60(7):1299–1348

Bucholz CE, Jagoutz O, Schmidt MW, Sambuu O (2014) Fractional crystallization of high-K arc magmas: biotite-versus amphibole-dominated fractionation series in the Dariv Igneous Complex, Western Mongolia. Contrib Miner Petrol 168(5):1072

Bucholz CE, Stolper EM, Eiler JM, Breaks FW (2018) A comparison of oxygen fugacities of strongly peraluminous granites across the Archean-Proterozoic boundary. J Petrol 59(11):2123–2156

Cawthorn RG, Brown PA (1976) A model for the formation and crystallization of corundum-normative calc-alkaline magmas through amphibole fractionation. J Geol 84(4):467–476

Cawthorn RG, O'Hara MJ (1976) Amphibole fractionation in calc-alkaline magma genesis. Am J Sci 276(3):309–329

Cervantes P, Wallace PJ (2003) Role of H2O in subduction-zone magmatism: new insights from melt inclusions in high-Mg basalts from central Mexico. Geology 31(3):235–238

Chapman AD, Saleeby JB, Wood DJ, Piasecki A, Kidder S, Ducea MN, Farley KA (2012) Late Cretaceous gravitational collapse of the southern Sierra Nevada batholith, California. Geosphere 8(2):314–341

Chapman JB, Gehrels GE, Ducea MN, Giesler N, Pullen A (2016) A new method for estimating parent rock trace element concentrations from zircon. Chem Geol 439:59–70

Christensen NI, Mooney WD (1995) Seismic velocity structure and composition of the continental crust: a global view. J Geophys Res Solid Earth 100(B6):9761–9788

Coleman D, Glazner A, Miller J, Bradford K, Frost T, Joye J, Bachl C (1995) Exposure of a Late Cretaceous layered mafic-felsic magma system in the central Sierra Nevada Batholith, California. Contrib Mineral Petrol 120(2):129–136

Debari SM, Sleep NH (1991) High-Mg, low-Al bulk composition of the Talkeetna island arc, Alaska: implications for primary magmas and the nature of arc crust. Geol Soc Am Bull 103(1):37–47

Debari S, Kay SM, Kay R (1987) Ultramafic xenoliths from Adagdak volcano, Adak, Aleutian Islands, Alaska: deformed igneous cumulates from the Moho of an island arc. J Geol 95(3):329–341

DeCelles PG, Ducea MN, Kapp P, Zandt G (2009) Cyclicity in Cordilleran orogenic systems. Nat Geosci 2(4):251–257

Dodge F, Calk L, Kistler R (1986) Lower crustal xenoliths, Chinese Peak lava flow, central Sierra Nevada. J Petrol 27(6):1277–1304

Dodge F, Lockwood J, Calk L (1988) Fragments of the mantle and crust from beneath the Sierra Nevada batholith: Xenoliths in a volcanic pipe near Big Creek, California. Geol Soc Am Bull 100(6):938–947

Domenick MA, Kistler RW, Dodge F, Tatsumoto M (1983) Nd and Sr isotopic study of crustal and mantle inclusions from the Sierra Nevada and implications for batholith petrogenesis. Geol Soc Am Bull 94(6):713–719

Draper DS, Johnston AD (1992) Anhydrous PT phase relations of an Aleutian high-MgO basalt: an investigation of the role of olivine-liquid reaction in the generation of arc high-alumina basalts. Contrib Miner Petrol 112(4):501–519

Ducea MN (2001) The California arc: thick granitic batholiths, eclogitic residues, lithospheric-scale thrusting, and magmatic flare-ups. GSA Today 11(11):4–10

Ducea MN, Saleeby JB (1996) Buoyancy sources for a large, unrooted mountain range, the Sierra Nevada, California: Evidence from xenolith thermobarometry. J Geophys Res Solid Earth 101(B4):8229–8244

Ducea M, Saleeby J (1998) A case for delamination of the deep batholithic crust beneath the Sierra Nevada, California. Int Geol Rev 40(1):78–93

Ducea MN, Paterson SR, DeCelles PG (2015) High-volume magmatic events in subduction systems. Elements 11(2):99–104

English JM, Johnston ST, Wang K (2003) Thermal modelling of the Laramide orogeny: testing the flat-slab subduction hypothesis. Earth Planet Sci Lett 214(3–4):619–632

Erdmann M, Koepke J (2016) Silica-rich lavas in the oceanic crust: experimental evidence for fractional crystallization under low water activity. Contrib Miner Petrol 171(10):83

Fliedner MM, Klemperer SL, Christensen NI (2000) Three-dimensional seismic model of the Sierra Nevada arc, California, and its implications for crustal and upper mantle composition. J Geophys Res Solid Earth 105(B5):10899–10921

Frost TP (1987) Sample localities, radiometric ages, descriptions, and major-and trace-element abundances of Late Jurassic mafic plutonic rocks, eastern Sierra Nevada, California. Department of the Interior, US Geological Survey

Frost TP, Mahood GA (1987) Field, chemical, and physical constraints on mafic-felsic magma interaction in the Lamarck Granodiorite, Sierra Nevada, California. Geol Soc Am Bull 99(2):272–291

Ghiorso MS, Sack RO (1995) Chemical mass transfer in magmatic processes IV. A revised and internally consistent thermodynamic model for the interpolation and extrapolation of liquid-solid equilibria in magmatic systems at elevated temperatures and pressures. Contrib Mineral Petrol 119(2–3):197–212

Greene AR, DeBari SM, Kelemen PB, Blusztajn J, Clift PD (2006) A detailed geochemical study of island arc crust: the Talkeetna arc section, south–central Alaska. J Petrol 47(6):1051–1093

Grove TL, Elkins-Tanton LT, Parman SW, Chatterjee N, Müntener O, Gaetani GA (2003) Fractional crystallization and mantle-melting controls on calc-alkaline differentiation trends. Contrib Miner Petrol 145(5):515–533

Guo L, Jagoutz O, Shinevar WJ, Zhang HF (2020) Formation and composition of the Late Cretaceous Gangdese arc lower crust in southern Tibet. Contrib Miner Petrol 175:58

Hamada M, Fujii T (2008) Experimental constraints on the effects of pressure and H 2 O on the fractional crystallization of high-Mg island arc basalt. Contrib Miner Petrol 155(6):767–790

Hamada M, Okayama Y, Kaneko T, Yasuda A, Fujii T (2014) Polybaric crystallization differentiation of H 2 O-saturated island arc low-K tholeiite magmas: a case study of the Izu-Oshima volcano in the Izu arc. Earth Planets Space 66(1):1–10

Holland JE, Surpless B, Smith DR, Loewy SL, Lackey JS (2013) Intrusive history and petrogenesis of the Ash Mountain Complex, Sierra Nevada batholith, California (USA). Geosphere 9(4):691–717

Icenhower JP, London D (1997) Partitioning of fluorine and chlorine between biotite and granitic melt: experimental calibration at 200 MPa H 2 O. Contrib Miner Petrol 127(1–2):17–29

Jagoutz OE (2010) Construction of the granitoid crust of an island arc. Part II: a quantitative petrogenetic model. Contrib Mineral Petrol 160(3):359–381

Jagoutz O (2014) Arc crustal differentiation mechanisms. Earth Planet Sci Lett 396:267–277

Jagoutz O, Klein B (2018) On the importance of crystallization-differentiation for the generation of SiO2-rich melts and the compositional build-up of arc (and continental) crust. Am J Sci 318(1):29–63

Jagoutz OE, Burg J-P, Hussain S, Dawood H, Pettke T, Iizuka T, Maruyama S (2009) Construction of the granitoid crust of an island arc part I: geochronological and geochemical constraints from the plutonic Kohistan (NW Pakistan). Contrib Miner Petrol 158(6):739–755

Jones CH, Phinney RA (1998) Seismic structure of the lithosphere from teleseismic converted arrivals observed at small arrays in the southern Sierra Nevada and vicinity, California. J Geophys Res Solid Earth 103(B5):10065–10090

Kay SM, Kay R (1985) Role of crystal cumulates and the oceanic crust in the formation of the lower crust of the Aleutian arc. Geology 13(7):461–464

Kelley KA, Cottrell E (2009) Water and the oxidation state of subduction zone magmas. Science 325(5940):605–607

Kirsch M, Paterson SR, Wobbe F, Ardila AMM, Clausen BL, Alasino PH (2016) Temporal histories of Cordilleran continental arcs: testing models for magmatic episodicity. Am Miner 101(10):2133–2154

Klein BZ, Jagoutz OE (2021) Construction of a trans-crustal magma system: building the Bear Valley Intrusive Suite, southern Sierra Nevada, California. Earth Planet Sci Lett 553:116624

Köhler T, Brey G (1990) Calcium exchange between olivine and clinopyroxene calibrated as a geothermobarometer for natural peridotites from 2 to 60 kb with applications. Geochim Cosmochim Acta 54(9):2375–2388

Krawczynski MJ, Grove TL, Behrens H (2012) Amphibole stability in primitive arc magmas: effects of temperature, H 2 O content, and oxygen fugacity. Contrib Miner Petrol 164(2):317–339

Kress VC, Carmichael IS (1991) The compressibility of silicate liquids containing Fe2O3 and the effect of composition, temperature, oxygen fugacity and pressure on their redox states. Contrib Miner Petrol 108(1–2):82–92

Lackey JS, Valley JW, Saleeby JB (2005) Supracrustal input to magmas in the deep crust of Sierra Nevada batholith: evidence from high-δ18O zircon. Earth Planet Sci Lett 235(1–2):315–330

Lackey JS, Valley JW, Chen JH, Stockli DF (2008) Dynamic magma systems, crustal recycling, and alteration in the central Sierra Nevada batholith: the oxygen isotope record. J Petrol 49(7):1397–1426

Leake BE, Woolley AR, Arps CE, Birch WD, Gilbert MC, Grice JD, Hawthorne FC, Kato A, Kisch HJ, Krivovichev VG (1997) Nomenclature of amphiboles; report of the subcommittee on amphiboles of the International Mineralogical Association, Commission on New Minerals and Mineral Names. Can Mineral 35(1):219–246

Lee C-T, Rudnick RL, Brimhall GH Jr (2001) Deep lithospheric dynamics beneath the Sierra Nevada during the Mesozoic and Cenozoic as inferred from xenolith petrology. Geochem Geophys Geosyst. https://doi.org/10.1029/2001GC000152

Lee C-TA, Cheng X, Horodyskyj U (2006) The development and refinement of continental arcs by primary basaltic magmatism, garnet pyroxenite accumulation, basaltic recharge and delamination: insights from the Sierra Nevada, California. Contrib Mineral Petrol 151(2):222–242

Lockwood J, Bateman P (1976) Geologic map of the Shaver Lake 15-minute quadrangle, central Sierra Nevada, California: US Geological Survey. Geologic Quadrangle Map GQ-1271, scale 1(62,500)

Loucks RR, Fiorentini ML, Henríquez GJ (2020) New magmatic oxybarometer using trace elements in zircon. J Petrol 61(3)

Mason RA (1992) Models of order and iron-fluorine avoidance in biotite. Can Mineral 30(2):343–354

Mayo EB (1941) Deformation in the interval Mt. Lyell-Mt. Whitney, California. Bull Geol Soc Am 52(7):1001–1084

McCarthy A, Müntener O (2016) Comb layering monitors decompressing and fractionating hydrous mafic magmas in subvolcanic plumbing systems (Fisher Lake, Sierra Nevada, USA). J Geophys Res Solid Earth 121(12):8595–8621

Melekhova E, Blundy J, Robertson R, Humphreys MC (2015) Experimental evidence for polybaric differentiation of primitive arc basalt beneath St. Vincent, Lesser Antilles. J Petrol 56(1):161–192

Middlemost EA (1994) Naming materials in the magma/igneous rock system. Earth Sci Rev 37(3–4):215–224

Miller DM, Goldstein SL, Langmuir CH (1994) Cerium/lead and lead isotope ratios in arc magmas and the enrichment of lead in the continents. Nature 368(6471):514–520

Mukhopadhyay B (1991) Garnet breakdown in some deep seated garnetiferous xenoliths from the central Sierra Nevada: petrologic and tectonic implications. Lithos 27(1):59–78

Mukhopadhyay B, Manton W (1994) Upper-mantle fragments from beneath the Sierra Nevada Batholith: partial fusion, fractional crystallization, and metasomatism in a subduction related ancient lithosphere. J Petrol 35(5):1417–1450

Müntener O, Ulmer P (2018) Arc crust formation and differentiation constrained by experimental petrology. Am J Sci 318(1):64–89

Müntener O, Kelemen PB, Grove TL (2001) The role of H2O during crystallization of primitive arc magmas under uppermost mantle conditions and genesis of igneous pyroxenites: an experimental study. Contrib Miner Petrol 141(6):643–658

Mutch E, Blundy J, Tattitch B, Cooper F, Brooker R (2016) An experimental study of amphibole stability in low-pressure granitic magmas and a revised Al-in-hornblende geobarometer. Contrib Miner Petrol 171(10):85

Nadin ES, Saleeby JB, Wright J, Shervais J (2008) Disruption of regional primary structure of the Sierra Nevada batholith by the Kern Canyon fault system, California. Geol Soc Am-Special Papers 438:429

Nadin ES, Saleeby JB, Wong M (2016) Thermal evolution of the Sierra Nevada batholith, California, and implications for strain localization. Geosphere 12(2):377–399

Nandedkar RH, Ulmer P, Müntener O (2014) Fractional crystallization of primitive, hydrous arc magmas: an experimental study at 0.7 GPa. Contrib Mineral Petrol 167(6):1015

Otamendi JE, Ducea MN, Bergantz GW (2012) Geological, petrological and geochemical evidence for progressive construction of an arc crustal section, Sierra de Valle Fertil, Famatinian Arc, Argentina. J Petrol 53(4):761–800

Peselnick L, Lockwood JP, Stewart R (1977) Anisotropic elastic velocities of some upper mantle xenoliths underlying the Sierra Nevada batholith. J Geophys Res 82(14):2005–2010

Pickett DA, Saleeby JB (1993) Thermobarometric constraints on the depth of exposure and conditions of plutonism and metamorphism at deep levels of the Sierra Nevada batholith, Tehachapi Mountains, California. J Geophys Res Solid Earth 98(B1):609–629

Portnyagin M, Hoernle K, Plechov P, Mironov N, Khubunaya S (2007) Constraints on mantle melting and composition and nature of slab components in volcanic arcs from volatiles (H2O, S, Cl, F) and trace elements in melt inclusions from the Kamchatka Arc. Earth Planet Sci Lett 255(1–2):53–69

Putirka KD (2008) Thermometers and barometers for volcanic systems. Rev Mineral Geochem 69(1):61–120

Ratajeski K, Glazner AF, Miller BV (2001) Geology and geochemistry of mafic to felsic plutonic rocks in the Cretaceous intrusive suite of Yosemite Valley, California. Geol Soc Am Bull 113(11):1486–1502

Reid JB Jr, Evans OC, Fates DG (1983) Magma mixing in granitic rocks of the central Sierra Nevada, California. Earth Planet Sci Lett 66:243–261

Rezeau H, Klein BZ, Jagoutz O (2021) Mixing dry and wet magmas in the lower crust of a continental arc: new petrological insights from the Bear Valley Intrusive Suite, southern Sierra Nevada, California. Contrib Mineral Petrol. https://doi.org/10.1007/s00410-021-01832-2

Ross DC (1985) Mafic: gneissic complex (batholithic root?) in the southernmost Sierra Nevada, California. Geology 13(4):288–291

Rowe MC, Kent AJ, Nielsen RL (2009) Subduction influence on oxygen fugacity and trace and volatile elements in basalts across the Cascade Volcanic Arc. J Petrol 50(1):61–91

Ruppert S, Fliedner MM, Zandt G (1998) Thin crust and active upper mantle beneath the southern Sierra Nevada in the western United States. Tectonophysics 286(1–4):237–252

Saleeby J, Ducea MN, Busby C, Nadin E, Wetmore PH, Wright J, Shervais J (2008) Chronology of pluton emplacement and regional deformation in the southern Sierra Nevada batholith, California. Geol Soc Am - Special Papers 438:397

Sams DB, Saleeby JB (1988) Geology and petrotectonic significance of crystalline rocks of the southernmost Sierra Nevada, California. In: Ernst WG (ed) Metamorphism and Crustal Evolution of the Western United States (Rubey Volume 7): Prentice Hall Inc 865:893

Schmidt MW, Jagoutz O (2017) The global systematics of primitive arc melts. Geochem Geophys Geosyst 18(8):2817–2854

Sisson T, Grove T (1993) Experimental investigations of the role of H 2 O in calc-alkaline differentiation and subduction zone magmatism. Contrib Miner Petrol 113(2):143–166

Sisson T, Layne G (1993) H2O in basalt and basaltic andesite glass inclusions from four subduction-related volcanoes. Earth Planet Sci Lett 117(3–4):619–635

Sisson T, Grove T, Coleman D (1996) Hornblende gabbro sill complex at Onion Valley, California, and a mixing origin for the Sierra Nevada batholith. Contrib Miner Petrol 126(1–2):81–108

Sisson T, Ratajeski K, Hankins W, Glazner AF (2005) Voluminous granitic magmas from common basaltic sources. Contrib Miner Petrol 148(6):635–661

Soesoo A (2000) Fractional crystallization of mantle-derived melts as a mechanism for some I-type granite petrogenesis: an example from Lachlan Fold Belt, Australia. J Geol Soc 157(1):135–149

Sparks R, Marshall L (1986) Thermal and mechanical constraints on mixing between mafic and silicic magmas. J Volcanol Geotherm Res 29(1–4):99–124

Stolz A, Jochum K, Spettel B, Hofmann A (1996) Fluid-and melt-related enrichment in the subarc mantle: evidence from Nb/Ta variations in island-arc basalts. Geology 24(7):587–590

Sun SS, McDonough WF (1989) Chemical and isotopic systematics of oceanic basalts: implications for mantle composition and processes. Geol Soc Lond, Special Publications 42(1):313–345

Ulmer P, Kaegi R, Müntener O (2018) Experimentally derived intermediate to silica-rich arc magmas by fractional and equilibrium crystallization at 1· 0 GPa: an evaluation of phase relationships, compositions, liquid lines of descent and oxygen fugacity. J Petrol 59(1):11–58

Villiger S, Ulmer P, Müntener O, Thompson AB (2004) The liquid line of descent of anhydrous, mantle-derived, tholeiitic liquids by fractional and equilibrium crystallization—an experimental study at 1· 0 GPa. J Petrol 45(12):2369–2388

Walker BA, Bergantz GW, Otamendi JE, Ducea MN, Cristofolini EA (2015) A MASH zone revealed: the mafic complex of the Sierra Valle Fértil. J Petrol 56(9):1863–1896

Waters LE, Lange RA (2015) An updated calibration of the plagioclase-liquid hygrometer-thermometer applicable to basalts through rhyolites. Am Miner 100(10):2172–2184